

# Carbon-Based Supercapacitors Produced by Activation of Graphene

Yanwu Zhu,<sup>1</sup> Shanthi Murali,<sup>1</sup> Meryl D. Stoller,<sup>1</sup> K. J. Ganesh,<sup>1</sup> Weiwei Cai,<sup>1</sup> Paulo J. Ferreira,<sup>1</sup> Adam Pirkle,<sup>2</sup> Robert M. Wallace,<sup>2</sup> Katie A. Cychosz,<sup>3</sup> Matthias Thommes,<sup>3</sup> Dong Su,<sup>4</sup> Eric A. Stach,<sup>4</sup> Rodney S. Ruoff<sup>1\*</sup>

Supercapacitors, also called ultracapacitors or electrochemical capacitors, store electrical charge on high-surface-area conducting materials. Their widespread use is limited by their low energy storage density and relatively high effective series resistance. Using chemical activation of exfoliated graphite oxide, we synthesized a porous carbon with a Brunauer-Emmett-Teller surface area of up to 3100 square meters per gram, a high electrical conductivity, and a low oxygen and hydrogen content. This  $sp^2$ -bonded carbon has a continuous three-dimensional network of highly curved, atom-thick walls that form primarily 0.6- to 5-nanometer-width pores. Two-electrode supercapacitor cells constructed with this carbon yielded high values of gravimetric capacitance and energy density with organic and ionic liquid electrolytes. The processes used to make this carbon are readily scalable to industrial levels.

Supercapacitors store energy by forming a double layer of electrolyte ions on the surface of conductive electrodes. Supercapacitors are not limited by the electrochemical charge transfer kinetics of batteries and thus can operate at very high charge and discharge rates and can have lifetimes of over a million cycles (1). However, the energy stored in supercapacitors is currently an order of magnitude lower than that of batteries, which limits their adoption to those applications that require high cycle life and power density. The energy density of existing state-of-the-art supercapacitor devices, which are mainly based on porous activated carbon (AC), is about 4 to 5 watt-hour (Wh)/kg, whereas that of lead acid batteries is in the range of 26 to 34 Wh/kg (2). A typical AC material, with a Brunauer-Emmett-Teller (BET) specific surface area (SSA) in the range of 1000 to 2000  $m^2/g$  and a pore size distribution in the range of 2 to 5 nm, has a gravimetric capacitance of 100 to 120 F/g in organic electrolytes (3). Research has thus been focused on increasing energy density without sacrificing cycle life or high power density (4). An increased capacitance in the organic electrolyte tetraethylammonium tetrafluoroborate ( $TEA BF_4$ ) in acetonitrile (AN) by using carbide-derived carbons (CDCs) has been reported (5). Metal oxides such as  $RuO_2$  or  $MnO_2$  (6),  $MoO_3$  (7), and electronically conducting polymers (8), or their composites, have been used to increase specific

capacitance via pseudo-capacitive redox reactions. Although capacitances of up to 1300 F/g (such as with  $MnO_2$ ) have been reported in aqueous electrolytes (9), the low electrical conductance, poor

compatibility with organic electrolytes, and short cycle life have limited the practical application of these pseudo-capacitive materials. Carbon nanotubes (CNTs), especially single-walled CNTs (SWNTs), have an ideal limit SSA of 1300  $m^2/g$  (10), can have high electrical conductance along the tubes, and demonstrate good performance in organic electrolyte (11). However, the high cost for mass production of high-quality SWNTs is a challenge for the commercialization of SWNT-based supercapacitors.

Graphene has a theoretical SSA of 2630  $m^2/g$  and a very high intrinsic electrical conductivity in plane as well as high mechanical strength and chemical stability (12). Graphene-based material derived from graphite oxide (GO) is now being manufactured in ton quantities at low cost (13). We have previously demonstrated supercapacitors that were based on reduced graphene oxide with capacitance values of approximately 130 and 100 F/g in aqueous KOH and organic electrolytes, respectively (14). With a low equivalent series resistance (ESR), the supercapacitor performance did not show much degradation with an increase in the scan rate. Various graphene-based materials derived from GO have reported

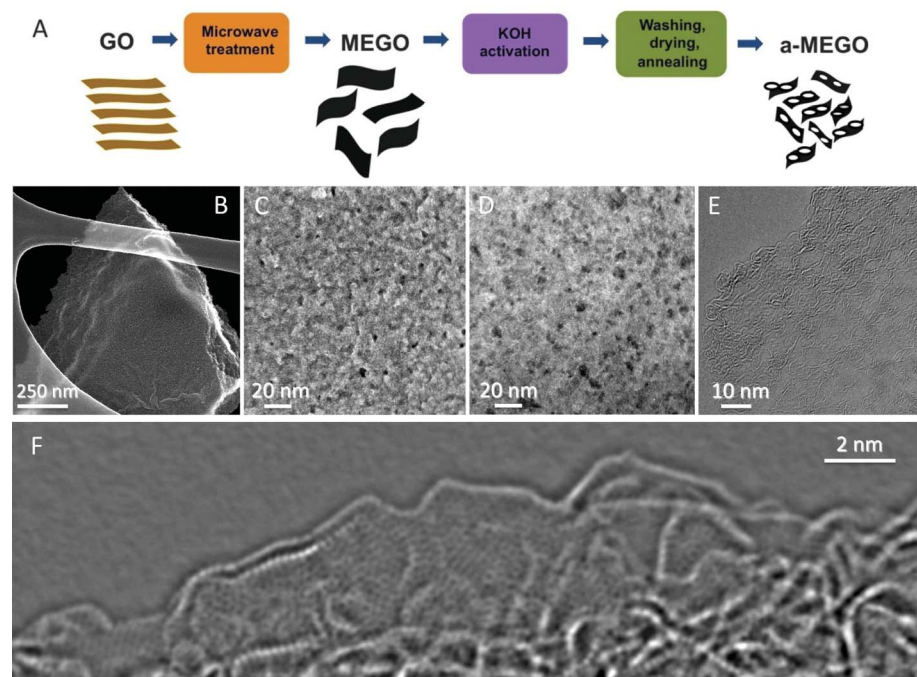


**Fig. 1.** (A) Schematic showing the microwave exfoliation/reduction of GO and the following chemical activation of MEGO with KOH that creates pores while retaining high electrical conductivity. (B) Low-magnification SEM image of a 3D a-MEGO piece. (C) High-resolution SEM image of a different sample region that demonstrates the porous morphology. (D) ADF-STEM image of the same area as (C), acquired simultaneously. As seen, a-MEGO contains micro- and mesopores with a distribution of sizes between ~1 and ~10 nm. (E) High-resolution phase contrast electron micrograph of the thin edge of an a-MEGO chunk, taken at 80 kV. There is a variation in focus across the image because of the sloped nature of the sample and changes in sample thickness. The image shows the presence of a dense network of nanometer-scale pores surrounded by highly curved, predominantly single-layer carbon. (F) Exit wave reconstructed HR-TEM image from the edge of a-MEGO. The in-plane carbon atoms are clearly resolved, and a variety of  $n$ -membered carbon rings can be seen. Substantial curvature of the single-carbon sheets is visible, with the in-plane crystallinity being preserved.

<sup>1</sup>Department of Mechanical Engineering and Materials Science and Engineering Program, University of Texas at Austin, One University Station C2200, Austin, TX 78712, USA.

<sup>2</sup>Department of Materials Science and Engineering, University of Texas at Dallas, 800 West Campbell Road, Richardson, TX 75080, USA.

<sup>3</sup>Quantachrome Instruments, 1900 Corporate Drive, Boynton Beach, FL 33426, USA. <sup>4</sup>Center for Functional Nanomaterials, Brookhaven National Laboratory, Upton, NY 11973, USA.

\*To whom correspondence should be addressed. E-mail: r.ruoff@mail.utexas.edu

high-end capacitance values of  $\sim 200$  F/g in aqueous electrolytes (15, 16),  $\sim 120$  F/g in organic electrolytes (16, 17), and  $\sim 75$  F/g in an ionic liquid (18). Recently, supercapacitors using oriented graphene grown on nickel by means of chemical vapor deposition were reported (19) that demonstrated efficient filtering of 120 Hz current with a resistance capacitance (RC) time constant of less than 0.2 ms, but at the cost of effective energy storage because of the very low density of the electrode material.

To date, the reported SSA values of carbon materials derived from GO have been well below 2630  $\text{m}^2/\text{g}$ . Here, we report a simple activation with KOH of microwave exfoliated GO (MEGO) and thermally exfoliated GO (TEGO) to achieve SSA values up to 3100  $\text{m}^2/\text{g}$ . As described in (20), we prepared MEGO powders by irradiating GO in a microwave oven. The as-made MEGO powder was then placed in KOH solution, followed by filtration and drying, to form a series of MEGO/KOH mixtures for chemical activation. Each MEGO/KOH mixture was put in a tube furnace under flowing argon at a pressure of about 400 torr and heated at 800°C for 1 hour. A schematic of this activation process is shown in Fig. 1A. Chemical activation has been extensively used to obtain porous ACs (21). KOH activation has been used on CNTs (22), carbon nanofibers (23), and polyacrylonitrile-carbon nanotube composites (24), and improved porosity and enhanced supercapacitor performance were reported. It is suggested that the activation of carbon with KOH (25) proceeds as  $6\text{KOH} + \text{C} \leftrightarrow 2\text{K} + 3\text{H}_2 + 2\text{K}_2\text{CO}_3$ , followed by decomposition of  $\text{K}_2\text{CO}_3$  and/or reaction of  $\text{K}/\text{K}_2\text{CO}_3/\text{CO}_2$  with carbon.

The activation with KOH generated nanoscale pores in the product carbon. The SSA of the activated MEGO (a-MEGO) could be readily controlled by the ratio of KOH versus MEGO (fig. S1). The scanning electron microscopy (SEM) image in Fig. 1B shows the morphology of a typical a-MEGO piece. Figure 1 shows high-resolution SEM (Fig. 1C), annular dark field scanning trans-

mission electron microscopy (ADF-STEM) (Fig. 1D), and high-resolution TEM (HR-TEM) (Fig. 1, E and F) images of the microstructure. These images [and additional images (fig. S2 and movie S1)] clearly indicate that the activation process etches the MEGO and has generated a three-dimensional (3D) distribution of what are referred to as meso- and micropores in the porous materials literature. The activation with KOH yields a continuous 3D network of pores of extremely small size, ranging from  $\sim 1$  nm to  $\sim 10$  nm. Thus, it appears that the chemical activation is not merely digesting the MEGO but also dramatically restructuring it. (The 3D nature of these very small pores makes a statistically accurate quantitative analysis with EM of the distribution of pore sizes difficult because not all pores are visible in a given image.) The spherical aberration-corrected HR-TEM image presented as Fig. 1E (taken at 80 kV so as to prevent electron beam damage) further corroborates a dense pore structure with a continuous three-dimensional network of highly curved, predominantly atom-thick walls. An exit-wave reconstructed image (Fig. 1F) taken with the Transmission Electron Aberration-Corrected Microscope (TEAM) instrument (spherical and chromatic aberration correction, at 80 kV) clearly resolves the individual carbon atoms in the structure. This image shows that a-MEGO is composed of  $n$ -membered rings in plane, with  $n$  varying between 5 and 8. Additionally, it is clear that even as the walls bend through high degrees of curvature the in-plane crystallinity is preserved.

Electron paramagnetic resonance (EPR) data (fig. S3) indicate an unpaired spin count at the parts-per-million level. This—in hand with the very low H and O content in the a-MEGO indicated by elemental analysis—shows that a-MEGO has a small fraction of edge atoms. (If a large fraction of the C were edge atoms, they would either be functionalized or would be present as “dangling bonds” that would register an EPR signal.)

Characterization of a sample of a-MEGO by means of synchrotron powder x-ray diffraction (XRD) and x-ray photoelectron spectroscopy (XPS) is shown in Fig. 2, A and B. Comparison with MEGO indicates that the (002) peak of a-MEGO has a markedly reduced intensity and is dramatically broadened. These results are consistent with the observations from HR-TEM, which indicate that a-MEGO is composed of predominantly single-carbon sheets: Thus, a strong decrease in the (002) peak would be expected. A large increase in the low-angle scatter from a-MEGO versus MEGO is also noted, which is consistent with the presence of a high density of pores. In the XPS  $\text{C}1s$  spectrum of MEGO shown in Fig. 2B, the tail between 286 and 290 eV is due to C-O groups and energy loss “shake-up” features (26). These oxygen-containing groups were strongly suppressed after activation, with two new peaks appearing between 292 and 296 eV in the a-MEGO sample that were assigned as  $\text{K}2p$  peaks. The  $\text{K}2p$  peaks ( $<2$  atomic % as determined from XPS) in a-MEGO are due to potassium residue, primarily as  $\text{K}_2\text{CO}_3$  with a small amount of KOH. Quantification of the amount of  $\text{sp}^2$ -bonding can be determined by measuring the ratio between  $\pi^*$  bonding and  $\pi^* + \delta^*$  bonding by using electron energy loss spectroscopy (EELS) (27). A comparison of the carbon K near-edge structure for a-MEGO and graphite of equivalent thickness is presented in Fig. 2C. With the assumption that the  $\text{sp}^2$  bonding in the graphite reference spectra is 100%, the a-MEGO was found to have 98% ( $\pm 2\%$ )  $\text{sp}^2$  bonding. Complementary measurements were also made by XPS, reaching similar conclusions (further details of the fitting procedures can be found in fig. S4). Micro Raman spectroscopy (fig. S5A) and Fourier transform infrared spectroscopy (fig. S5B) are provided for completeness but did not supply additional insights about a-MEGO beyond the other methods of analysis discussed here.

State-of-the-art surface and pore-size characterization of the a-MEGO was performed by

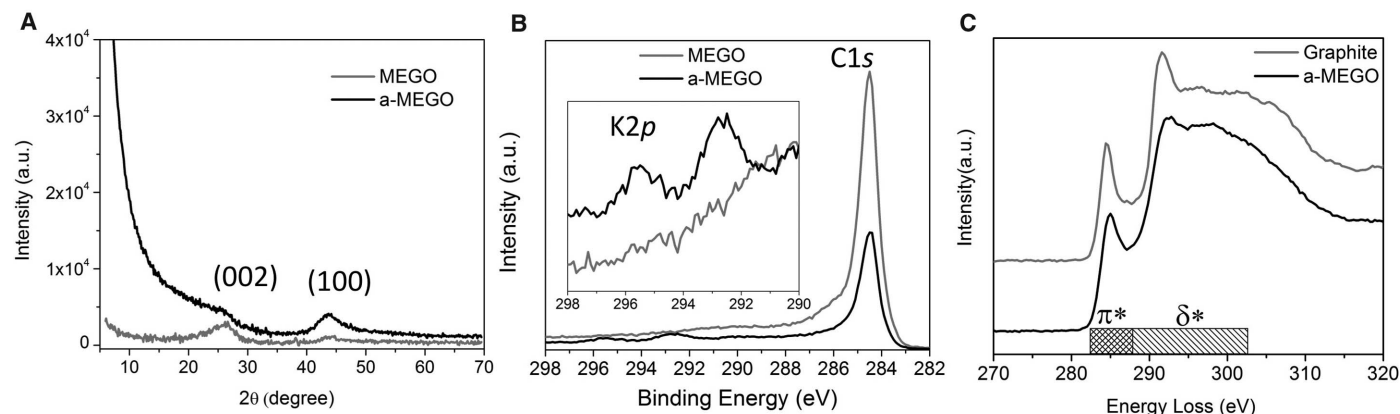


**Fig. 2.** Characterization of the a-MEGO material (SSA  $\sim 2520$   $\text{m}^2/\text{g}$ ) with MEGO or graphite as a control. **(A)** Synchrotron powder XRD pattern (plotted as  $\text{Cu K}\alpha$ ). Full width at half maximum of the (100) peak is  $\sim 2$  degrees for both samples, indicating average in-plane crystal size of  $\sim 5$  nm with the Scherrer equation; the

reduction of the (002) in a-MEGO indicates that there are essentially no inter-layer correlations of the carbon sheets. **(B)** XPS  $\text{C}1s$  spectra, with  $\text{K}2p$  region in the inset. **(C)** EELS spectra from a-MEGO and graphite. Quantification of the near-edge structure indicates that the a-MEGO has 98% ( $\pm 2\%$ )  $\text{sp}^2$  bonding.

coupling high-resolution nitrogen (77.4 K) and argon (87.3 K) adsorption/desorption experiments with advanced methods based on density functional theory (DFT) (28). In addition, CO<sub>2</sub> adsorption at 273.2 K has been performed to assess the ultramicropores (pores of width <1 nm). These isotherms, as shown in Fig. 3A, reveal the details of the low-pressure region in which micropore filling occurs, as well as the linear plot of the argon and nitrogen isotherms that reveal pore condensation and type H2 hysteresis [according to the International Union of Pure and Applied Chemistry (IUPAC) classification] (29) for the a-MEGO sample, which is indicative of an interconnected pore system exhibiting constrictions (29, 30). For comparison, nitrogen adsorption on a MEGO control sample is also shown in fig. S6, and it is evident that the pore volume of MEGO is much smaller than that of a-MEGO; the small overall pore volume should be caused by the platelet-like structure in MEGO—likely just the gap between platelets (20). In contrast, the pores in a-MEGO have a well-defined micro-mesopore size distribution as shown in Fig. 3B, with a huge increase in pore volume (up to 2.14 cm<sup>3</sup>/g) relative to MEGO. The a-MEGO had a high nitrogen BET SSA of ~3100 m<sup>2</sup>/g (calculated in the linear relative pressure range from 0.1 to 0.3). Within this context, in a strict sense the BET method is not applicable to microporous solids, and hence the obtained BET surface area should be considered as an apparent or equivalent area only. Figure 3B displays the results of the cumulative pore volume and pore size analysis from CO<sub>2</sub> and nitrogen adsorption by applying a hybrid nonlocal DFT (NLDFIT) kernel, assuming a slit pore geometry for the micropores and a cylindrical-pore geometry for the mesopores, which appears (although oversimplified) to be a reasonable as-

sumption also with regard to the SEM/STEM/TEM results. The obtained pore-size/volume distribution indicates that this carbon sample is distinctive because of the existence of well-defined micro- and mesopores. The presence of ultramicropores is seen from the CO<sub>2</sub> data, and the analysis of the nitrogen adsorption data reveals the presence of micropores in the ~1-nm size range as well as narrow mesopores centered around 4 nm in size. The latter is in good agreement with the bimodal distribution of pore sizes observed with high-resolution EM images. A quenched solid DFT (QSDFT), which quantitatively accounts for the surface roughness (31), also has been used to obtain the pore-size distribution of a-MEGO from the nitrogen and argon adsorption data, as shown in fig. S7. The pore size distribution curves obtained from argon and nitrogen agree very well.

Using best-practice methods for determining an electrode material's performance for supercapacitors (32), we constructed and measured the performance of two-electrode symmetrical supercapacitor cells on the basis of a-MEGO (SSA ~ 2400 m<sup>2</sup>/g) and 1-butyl-3-methyl-imidazolium tetrafluoroborate (BMIM BF<sub>4</sub>)/AN electrolyte, as shown in Fig. 4. The cyclic voltammetry (CV) testing (Fig. 4A) shows rectangular curves from 0 to 3.5 V over a wide range of voltage scan rates. The galvanostatic charge/discharge curves at three current densities are shown in Fig. 4B. The specific capacitance was calculated from the discharge curves with values of 165, 166, and 166 F/g obtained at current densities of 1.4, 2.8, and 5.7 A/g, respectively. The corresponding volumetric capacitance is ~60 F/cm<sup>3</sup>. The voltage drop at the initiation of the discharge is 0.034 V (for the current density of 1.4 A/g), suggesting a very low ESR in the test cell. A frequency response analysis (FRA) of the frequency range from 500 kHz

to 5 mHz yields the Nyquist plot shown in Fig. 4C. The plot features a vertical curve, indicating a nearly ideal capacitive behavior of the cell. From the magnified data in the high-frequency range (Fig. 4C, inset), a transition between the RC semi-circle and the migration of electrolyte was observed at a frequency of about 382 Hz, corresponding to a resistance of 2.45 ohms. The diffusion of electrolyte ions stopped at about 3 Hz, and thereafter the whole capacitance was reached (33). The voltage drop at the beginning of discharge curves was used to estimate the internal resistance. An ESR of 3.2 ohms was obtained from a-MEGO in the BMIM BF<sub>4</sub>/AN electrolyte. Based on a series RC model, the capacitance from the FRA data as a function of frequency is shown in Fig. 4D. The capacitance decreases sharply at about 4 Hz and remains 0.035 F at 10 Hz. Supercapacitor performance of the a-MEGO (SSA ~ 3100 m<sup>2</sup>/g) in the TEA BF<sub>4</sub>/AN electrolyte was also measured and yielded a specific capacitance of above 150 F/g as obtained from the discharge curve with a constant current of 0.8 A/g, with an ESR of 4.6 ohms (fig. S8). One other carbon (KOH-activated CDCs) using the same AN-based electrolyte with comparable specific capacitance values has been reported (34). a-MEGO has the highest gravimetric capacitance in organic electrolyte reported to date for any carbons derived from graphene-based materials.

Values for energy and power density were estimated on the basis of the supercapacitor measurements in the BMIM BF<sub>4</sub>/AN electrolyte. Using the specific capacitance value of 166 F/g (from the discharge curve with a constant current of 5.7 A/g) and working voltage of 3.5 V, the energy density is ~70 Wh/kg for the a-MEGO in the cell. Based on a weight ratio of 30% for the active electrode material in a packaged supercapacitor device—typical

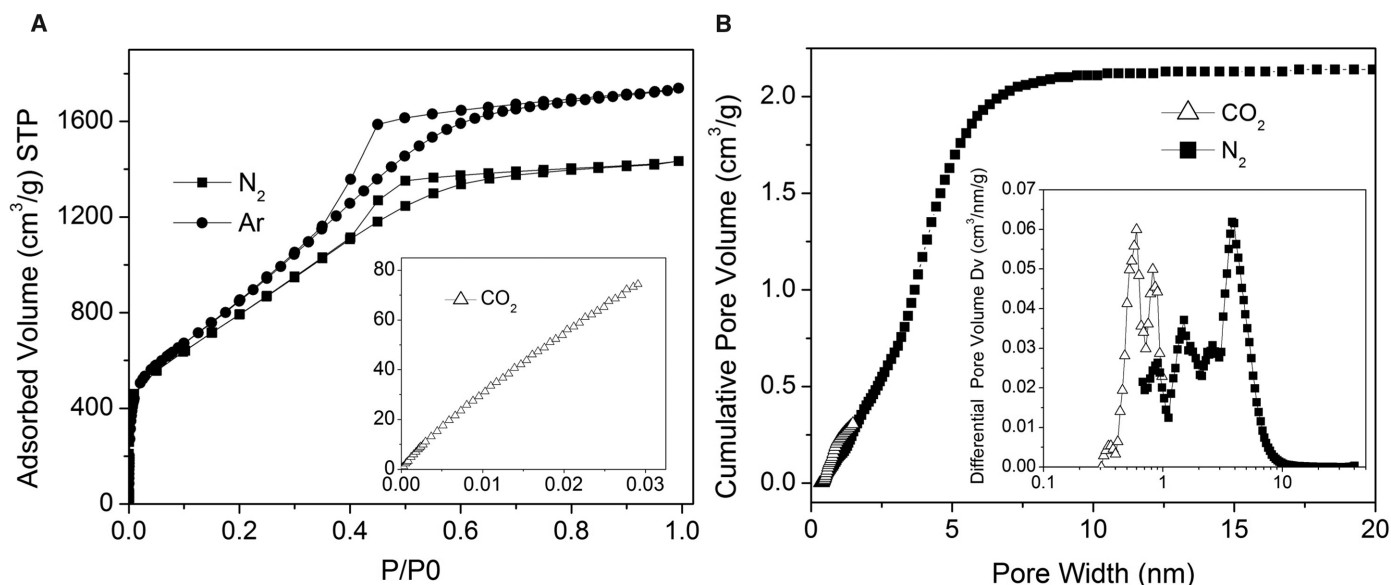


**Fig. 3.** Gas adsorption/desorption analysis of an a-MEGO sample (SSA ~ 3100 m<sup>2</sup>/g). **(A)** High-resolution, low-pressure N<sub>2</sub> (77.4 K) and Ar (87.3 K) isotherms. **(Inset)** The CO<sub>2</sub> (273.2 K) isotherm. **(B)** Cumulative pore

volume and **(inset)** pore-size distribution for N<sub>2</sub> (calculated by using a slit/cylindrical NLDFIT model) and CO<sub>2</sub> (calculated by using a slit pore NLDFIT model).



for large-scale AC-based supercapacitors—a practical energy density of above 20 Wh/kg for a packaged device is expected. This is four times higher than existing AC-based supercapacitors, two times higher than that reported for carbon-oxide hybrid electrochemical devices (2), and nearly equal to the energy density of lead acid batteries. At the same current density (5.7 A/g), the power density is also very high at ~250 kW/kg, as estimated by using the voltage drop and ESR obtained from the discharge curve. For a packaged cell, the power density of ~75 kW/kg is one order higher than the values from commercial carbon supercapacitors that have energy density values of 4 to 5 Wh/kg (2). This material is also very stable. After 10,000 constant current charge/discharge cycles at a current density of 2.5 A/g in neat BMIM BF<sub>4</sub> electrolyte (fig. S9), 97% of its capacitance was retained. We reasoned that this carbon might perform even better with smaller-diameter ions (35). With neat ethyl-methyl-

imidazolium bis(trifluoromethylsulfonyl)imide (EMIM TFSI) as electrolyte (fig. S10), the measured gravimetric capacitance of a-MEGO (SSA ~ 3100 m<sup>2</sup>/g) at 3.5 V and a current density of 0.7 A/g is 200 F/g, with an ESR of 8.6 ohms. However, the curves in fig. S10 are not as ideal as those from a-MEGO in either BMIM BF<sub>4</sub>/AN or TEA BF<sub>4</sub>/AN electrolyte. Other carbons (such as CDCs) using the EMIM TFSI electrolyte have been reported with comparable performance values, although the measurements were performed at an elevated temperature (60°C) (36).

The high powder conductivity of ~500 S/m, a C/O atomic ratio of up to ~35, the very low H content, and the essential absence of dangling bonds in the a-MEGO suggest that it has a high content of sp<sup>2</sup>-bonded carbon and very few edge atoms for the samples with SSA of above 2500 m<sup>2</sup>/g. This along with the SEM, TEM, STEM, EELS, EPR, XPS, XRD, and adsorption isotherm data thus support a highly porous carbon comprised

almost entirely of single sheets of sp<sup>2</sup>-bonded carbon. This suggests that a large fraction of “negative curvature carbon” (37–39) could be present.

The excellent performance obtained for various electrolytes opens the possibility to engineer supercapacitor electrodes based on this form of carbon in order to target a wide range of applications, such as high energy, high power, or low cost. Unlike other carbon materials, no special substrates or transfer procedures are required for synthesis. For supercapacitor manufacturing, this material can be treated the same as current commercial ACs. Electrodes used for testing were of the same thickness used in commercial cells, and testing was performed using commercial collectors, separators, binders, and electrolytes. As previously stated, the processes used to synthesize this carbon electrode material are readily scalable to industrial levels. For example, we have demonstrated that this simple activation process

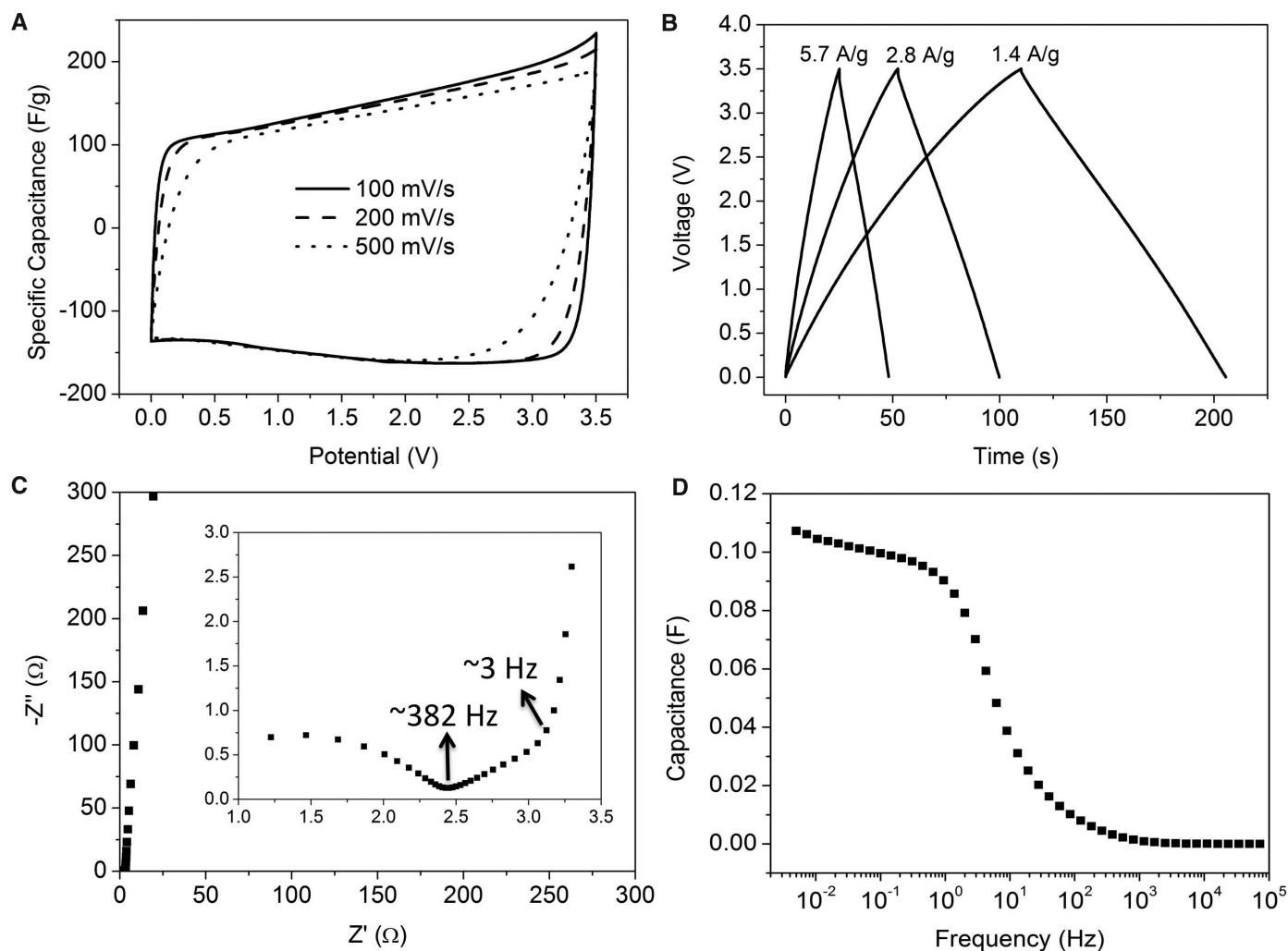


**Fig. 4.** Supercapacitor performance of a-MEGO (SSA ~ 2400 m<sup>2</sup>/g) in the BMIM BF<sub>4</sub>/AN electrolyte. **(A)** CV curves for different scan rates. Rectangular shapes indicate the capacitive behavior. **(B)** Galvanostatic charge/discharge curves of a-MEGO-based supercapacitor under different constant currents. **(C)** Nyquist plot, showing the imaginary part versus the real part of im-

pedance. (Inset) The data at high-frequency ranges, with frequency values corresponding to the transition of the curves marked. **(D)** Frequency response of the gravimetric capacitance of the a-MEGO supercapacitor. Capacitances of 35 and ~8.8 mF remain at the frequencies of 10 and 100 Hz, respectively.

also can be applied to TEGO (figs. S11 and S12), which is already being manufactured in ton quantities (13). By use of this type of simple activation process already commercially demonstrated for ACs, scaled a-MEGO and a-TEGO production for advanced energy/power electrochemical electrical energy storage devices may be realized in a short period.

## References and Notes

- J. R. Miller, P. Simon, *Science* **321**, 651 (2008).
- A. Burke, *Electrochim. Acta* **53**, 1083 (2007).
- J. A. Fernandez *et al.*, *J. Power Sources* **175**, 675 (2008).
- P. Simon, Y. Gogotsi, *Nat. Mater.* **7**, 845 (2008).
- J. Chmiola *et al.*, *Science* **313**, 1760 (2006).
- N. L. Wu, *Mater. Chem. Phys.* **75**, 6 (2002).
- T. Brezesinski, J. Wang, S. H. Tolbert, B. Dunn, *Nat. Mater.* **9**, 146 (2010).
- A. Rudge, J. Davey, I. Raistrick, S. Gottesfeld, J. P. Ferraris, *J. Power Sources* **47**, 89 (1994).
- M. Toupin, T. Brousse, D. Belanger, *Chem. Mater.* **16**, 3184 (2004).
- A. Izadi-Najafabadi *et al.*, *Adv. Mater.* **22**, E235 (2010).
- D. N. Futaba *et al.*, *Nat. Mater.* **5**, 987 (2006).
- Y. Zhu *et al.*, *Adv. Mater.* **22**, 3906 (2010).
- M. Segal, *Nat. Nanotechnol.* **4**, 612 (2009).
- M. D. Stoller, S. J. Park, Y. W. Zhu, J. H. An, R. S. Ruoff, *Nano Lett.* **8**, 3498 (2008).
- Y. Wang *et al.*, *J. Phys. Chem. C* **113**, 13103 (2009).
- W. Lv *et al.*, *ACS Nano* **3**, 3730 (2009).
- Y. Zhu *et al.*, *ACS Nano* **4**, 1227 (2010).
- S. R. C. Vivechand, C. S. Rout, K. S. Subrahmanyam, A. Govindaraj, C. N. R. Rao, *J. Chem. Sci.* **120**, 9 (2008).
- J. R. Miller, R. A. Outlaw, B. C. Holloway, *Science* **329**, 1637 (2010).
- Y. Zhu *et al.*, *Carbon* **48**, 2118 (2010).
- H. Marsh, F. Rodriguez-Reinoso, *Activated Carbon*. (Elsevier, London, 2006).
- E. Raymundo-Pinero *et al.*, *Carbon* **43**, 786 (2005).
- V. Barranco *et al.*, *J. Phys. Chem. C* **114**, 10302 (2010).
- T. Liu, T. V. Sreekumar, S. Kumar, R. H. Hauge, R. E. Smalley, *Carbon* **41**, 2440 (2003).
- M. A. Lillo-Rodenas, D. Cazorla-Amoros, A. Linares-Solano, *Carbon* **41**, 267 (2003).
- J. A. Leiro, M. H. Heinonen, T. Laiho, I. G. Batirev, *J. Electron Spectrosc. Relat. Phenom.* **128**, 205 (2003).
- S. D. Berger, D. R. McKenzie, P. J. Martin, *Philos. Mag. Lett.* **57**, 285 (1988).
- P. I. Ravikovitch, A. Vishnyakov, R. Russo, A. V. Neimark, *Langmuir* **16**, 2311 (2000).
- K. S. W. Sing *et al.*, *Pure Appl. Chem.* **57**, 603 (1985).
- J. C. Groen, L. A. A. Peffer, J. Perez-Ramirez, *Microporous Mesoporous Mater.* **60**, 1 (2003).
- A. V. Neimark, Y. Lin, P. I. Ravikovitch, M. Thommes, *Carbon* **47**, 1617 (2009).
- M. D. Stoller, R. S. Ruoff, *Energy Environ. Sci.* **3**, 1294 (2010).
- P. L. Taberna, P. Simon, J. F. Fauvarque, *J. Electrochem. Soc.* **150**, A292 (2003).
- C. Portet, M. A. Lillo-Rodenas, A. Linares-Solano, Y. Gogotsi, *Phys. Chem. Chem. Phys.* **11**, 4943 (2009).
- C. O. Ania, J. Pernak, F. Stefaniak, E. Raymundo-Pinero, F. Beguin, *Carbon* **44**, 3126 (2006).
- C. Largeot *et al.*, *J. Am. Chem. Soc.* **130**, 2730 (2008).
- S. J. Townsend, T. J. Lenosky, D. A. Muller, C. S. Nichols, V. Elser V, *Phys. Rev. Lett.* **69**, 921 (1992).
- H. Terrones, A. L. Mackay, *Prog. Cryst. Growth Charact. Mater.* **34**, 25 (1997).
- E. Barborini *et al.*, *Appl. Phys. Lett.* **81**, 3359 (2002).

**Acknowledgments:** We appreciate funding support from NSF under award DMR-0907324, the U.S. Department of Energy (DOE) under award DE-SC001951, and the Institute for Advanced Technology. The research by E.A. and D.S. has been carried out at the Center for Functional Nanomaterials, Brookhaven National Laboratory, which is supported by the DOE, Office of Basic Energy Sciences, under contract DE-AC02-98CH10886. We thank P. Stephens for XRD data collection, which is supported by DOE under contract DE-AC02-98CH10886, and P. Ercius for data collection on the TEAM instrument, supported by DOE contract DE-AC02-05CH11231. We thank M. Nilges for help with EPR. We thank J. Potts for providing graphite oxide samples. We appreciate use of equipment in K. Johnston's lab. R.M.W. and A.P. acknowledge the partial support of the GRC-NRI SWAN Center for the XPS data collection and analysis. R.S.R., Y.Z., M.D.S., and S.M. have filed a U.S. patent application (application no. PCT/US2011/036164) regarding work in this paper.

## Supporting Online Material

www.sciencemag.org/cgi/content/full/science.1200770/DC1  
SOM Text

Figs. S1 to S12

References

Movie S1

22 November 2010; accepted 2 May 2011

Published online 12 May 2011;

10.1126/science.1200770

# Disorder-Enhanced Transport in Photonic Quasicrystals

Liad Levi,\* Mikael Rechtsman,\* Barak Freedman, Tal Schwartz, Ofer Manela, Mordechai Segev†

Quasicrystals are aperiodic structures with rotational symmetries forbidden to conventional periodic crystals; examples of quasicrystals can be found in aluminum alloys, polymers, and even ancient Islamic art. Here, we present direct experimental observation of disorder-enhanced wave transport in quasicrystals, which contrasts directly with the characteristic suppression of transport by disorder. Our experiments are carried out in photonic quasicrystals, where we find that increasing disorder leads to enhanced expansion of the beam propagating through the medium. By further increasing the disorder, we observe that the beam progresses through a regime of diffusive-like transport until it finally transitions to Anderson localization and the suppression of transport. We study this fundamental phenomenon and elucidate its origins by relating it to the basic properties of quasicrystalline media in the presence of disorder.

Anderson localization (1), a fundamental concept in solid-state physics, describes how introducing disorder can transform a conducting crystal into an insulator. This prediction and subsequent experiments have shown that, generally, disorder works to arrest transport in periodic systems containing disorder (2–5), as well as in fully random potentials (6–10). However, some systems still pose fundamental challenges to this concept—most notably,

quasicrystals. Quasicrystals (QCs) (11, 12) constitute an intermediate phase between fully periodic and fully disordered media: They do not have a unit cell and do not exhibit translation symmetry; nevertheless, they possess noncrystallographic rotational symmetry and long-range order and display Bragg diffraction. Although many of the properties of QCs are now well understood, some fundamental questions remain. Perhaps one of the most intriguing questions related to QCs has to do with transport. Opposite to crystals containing disorder, which exhibit Anderson localization, it has been suggested that disorder can enhance transport in QCs (13, 14). Indirect experiments have indicated that in some regimes, increasing disorder could enhance transport (14).

The electronic structure of atomic QCs has been shown to have multifractal eigenstates (15, 16), which may or may not be normalizable (thus, localized), depending on the critical exponent associated with the given state. The transport properties of QCs are directly related to the critical nature of their eigenstates, in particular, in the presence of disorder (17). QCs have been shown to exhibit counterintuitive transport properties, including extremely low conductivity that increases with both temperature (inverse Matheisen rule) and spatial disorder arising from structural defects (14). Both of these effects have been attributed (16, 18) to hopping between critical states of different spatial extents near the Fermi energy (due to inelastic electron-phonon scattering for the former and elastic scattering from structural defects for the latter). This increase in transport with disorder is directly opposite to the characteristic behavior of crystals, wherein transport is reduced with increasing disorder.

Thus far, experiments on transport in atomic QCs were carried out by the study of macroscopic conductivity. However, conductivity experiments are problematic for addressing some basic questions on QCs. First, the mechanisms proposed to explain the unusual transport in QCs assume non-interacting electrons; however, conductivity measurements inevitably incorporate electron-electron interactions. Second, conductivity measurements do not allow direct observation of wave packets, which could be a key property in unraveling the mechanisms underlying transport. With the recent progress in photonic lattices (19), manifesting analogies between light propagating in a waveguide

Department of Physics and Solid State Institute, Technion, Haifa 32000, Israel.

\*These authors contributed equally to this work.

†To whom correspondence should be addressed. E-mail: msegev@tx.technion.ac.il



[www.sciencemag.org/cgi/content/full/science.1200770/DC1](http://www.sciencemag.org/cgi/content/full/science.1200770/DC1)

Supporting Online Material for

## **Carbon-Based Supercapacitors Produced by Activation of Graphene**

Yanwu Zhu, Shanthi Murali, Meryl D. Stoller, K. J. Ganesh, Weiwei Cai, Paulo J. Ferreira, Adam Pirkle, Robert M. Wallace, Katie A. Cychosz, Matthias Thommes, Dong Su, Eric A. Stach, Rodney S. Ruoff\*

\*To whom correspondence should be addressed. E-mail: [r.ruoff@mail.utexas.edu](mailto:r.ruoff@mail.utexas.edu)

Published 12 May 2011 on *Science Express*  
DOI: 10.1126/science.1200770

### **This PDF file includes:**

SOM Text

Figs. S1 to S12

References

**Other Supporting Online Material for this manuscript includes the following:**  
(available at [www.sciencemag.org/cgi/content/full/science.1200770/DC1](http://www.sciencemag.org/cgi/content/full/science.1200770/DC1))

Movie S1

Supporting Online Materials for

## **Carbon-based Supercapacitors Produced by Activation of Graphene**

Yanwu Zhu,<sup>1</sup> Shanthi Murali,<sup>1</sup> Meryl D. Stoller,<sup>1</sup> K. J. Ganesh,<sup>1</sup> Weiwei Cai,<sup>1</sup>  
Paulo J. Ferreira,<sup>1</sup> Adam Pirkle,<sup>2</sup> Robert M. Wallace,<sup>2</sup> Katie A. Cychosz,<sup>3</sup> Matthias  
Thommes,<sup>3</sup> Dong Su,<sup>4</sup> Eric A. Stach,<sup>4</sup> Rodney S. Ruoff<sup>1,\*</sup>

<sup>1</sup>Department of Mechanical Engineering and Materials Science and Engineering Program, The  
University of Texas at Austin, One University Station C2200, Austin, TX 78712

<sup>2</sup>Department of Materials Science and Engineering, The University of Texas at Dallas, 800 W.  
Campbell Rd, Richardson, TX 75080

<sup>3</sup>Quantachrome Instruments, 1900 Corporate Drive, Boynton Beach, FL 33426

<sup>4</sup>Center for Functional Nanomaterials, Brookhaven National Laboratory, Upton, NY 11973

\*E-mail: [r.ruoff@mail.utexas.edu](mailto:r.ruoff@mail.utexas.edu)

### **Table of Contents**

- 1. Synthesis of a-MEGO and a-TEGO from MEGO and TEGO**
- 2. Characterization methods**
- 3. Supercapacitor measurements**
- 4. Fig. S1: dependence of a-MEGO SSA on ratio of KOH to MEGO**
- 5. Fig. S2: SEM/STEM images of a-MEGO**
- 6. Fig. S3: EPR measurements of a-MEGO**
- 7. Fig. S4: XPS data for a-MEGO and analysis**
- 8. Fig. S5: Raman and FTIR analysis of a-MEGO**
- 9. Fig. S6: Comparison of N<sub>2</sub> BET data for MEGO and a-MEGO**
- 10. Fig. S7: QSDFT pore size distribution of a-MEGO**
- 11. Fig. S8: Supercapacitor performance of a-MEGO with TEA BF<sub>4</sub>/AN electrolyte**
- 12. Fig. S9: Stability testing of supercapacitor having a-MEGO with BMIM BF<sub>4</sub> electrolyte**
- 13. Fig. S10: Supercapacitor performance of a-MEGO with EMIM TFSI electrolyte**
- 14. Fig. S11: N<sub>2</sub> adsorption results for a-TEGO**
- 15. Fig. S12: Supercapacitor performance of a-TEGO with BMIM BF<sub>4</sub>/AN electrolyte**
- 16. Movies S1**
- 17. References**

## 1. Synthesis of a-MEGO and a-TEGO from MEGO and TEGO

The synthesis of microwave exfoliated graphite oxide (MEGO) followed the method described in Ref (1). Briefly, graphite oxide (GO) powders made from the modified Hummers' method were irradiated in a domestic microwave oven (GE, JES0736SM1SS) operated at 1100 W for 1 minute. During the irradiation, a large volume expansion of the GO powder occurred and the black, fluffy MEGO powder obtained was collected for activation. Typically, 400 mg MEGO powder was dispersed in 20 ml 7M aqueous KOH solution and stirred for 4 hours at a speed of 400 rpm, followed by another 20 hours of static soaking in ambient conditions. The extra KOH solution was removed by briefly filtering the mixture through a polycarbonate membrane (Whatman, 0.2  $\mu\text{m}$ ); then the mixture was dried in the lab environment at 65 °C for 24 hours. A control MEGO sample, made with the same soaking-drying process but with no KOH was also prepared, and 85% of the mass remained after drying. A KOH to MEGO ratio was calculated by assuming the MEGO in the dry MEGO/KOH mixture gave the same mass yield, i.e., 85%.

It was found that the KOH uptake (KOH/MEGO ratio) was linearly dependent on the molarity of the KOH solution, with other process parameters held constant (such as the amount of MEGO from the same batch of GO and the volume of KOH solution). For the MEGO soaked in 20 ml 7M KOH as described above, the KOH/MEGO ratio was  $8.9 \pm 0.3$ . The dry MEGO/KOH mixture was heated at 800 °C for 1 hour in a horizontal tube furnace (50-mm diameter), with an argon flow of 150 sccm and working pressure of  $\sim 400$  Torr. The temperature was ramped from room temperature to 800 °C at 5 °C/min. After cooling down in vacuum, the sample was repeatedly washed by de-ionized water until a pH value of 7 was reached. Then the sample was dried at 65 °C in ambient for 2 hours, followed by thermal annealing at 800 °C in vacuum (0.1 Torr) for 2 hours, to generate 'activated MEGO' (a-MEGO) powders. Thermally exfoliated graphite oxide ('TEGO'), made by 'thermal shocking' of GO at 250 °C in ambient (2), was activated following the same process. The a-MEGO and a-TEGO so obtained were characterized in a variety of ways, and supercapacitor measurements were made, as described in the main text and below.



## 2. Characterization methods

The a-MEGO was analyzed by scanning electron microscopy (SEM, Hitachi S5500, 30 kV), transmission electron microscopy (TEM, JEOL 2010F, 200 kV at UT-Austin; TEM, spherical aberration corrected FEI Titan 80/300, 80 kV at BNL; the spherical and chromatic aberration corrected TEAM instrument at LBNL, see: [ncem.lbl.gov/TEAM-project/](http://ncem.lbl.gov/TEAM-project/)) and scanning TEM (Aberration corrected Hitachi HD2700C at BNL). The exit wave reconstructed image shown in Figure 1F was processed using the MacTempas Exit Wave Reconstruction Package ([totalresolution.com](http://totalresolution.com)) from a series of 41 images, ranging from 28 nm above Gaussian to 28 nm below Gaussian and with 1.4 nm focal step size.

The measurement of the nitrogen adsorption isotherms was done with a Quantachrome Nova 2000 at 77.4 K to obtain the surface areas of a-MEGO samples from different KOH/MEGO ratios, and for the comparison between MEGO control and a-MEGO samples. Detailed adsorption experiments with nitrogen (77.4K), argon (87.3 K), and carbon dioxide (273.2 K) were also performed with a Quantachrome Autosorb iQ MP in order to assess surface area and pore characteristics of the a-MEGO. Nitrogen adsorption with the Quantachrome Autosorb iQ MP was also carried out on the a-TEGO. The samples were outgassed at 150 °C for 16 hours under turbomolecular vacuum pumping prior to the gas adsorption measurements.

Samples were sealed into glass Lindemann capillaries and x-ray diffraction patterns collected at the X12A beamline of the National Synchrotron Light Source, using x-rays of 0.699 Angstrom wavelength, in parallel beam geometry. Background from the glass was normalized at high angles, and the data converted to Cu K  $\alpha$  for the plot shown in Fig. 2A.

Micro Raman was done on a Witec Alpha 300 confocal Raman system with a laser wavelength of 532 nm. Lorentzian fitting was done to obtain the positions and widths of the D and G bands in the Raman shift spectra. Fourier transform infrared spectroscopy (FTIR) was done with a Perkin Elmer Spectrum BX.

X-ray photoelectron spectroscopy (XPS) was conducted with two separate systems equipped with monochromatic Al K $\alpha$  sources (Kratos AXIS Ultra DLD, Omicron Nanotechnology XM1000/EA 125 U7) to analyze the chemical composition of the samples.

Combustion elemental analysis was done at Atlantic Microlab, Inc. (Georgia, USA) for determination of the C, O, and H content. Electron paramagnetic resonance (EPR) measurements of a-MEGO were done with a Bruker EMX Plus (X band, 295 K) with 2,2-Di(4-tert-octylphenyl)-1-picrylhydrazyl (DPPH, Sigma Aldrich 257612) as a standard.

Electron energy loss spectroscopy (EELS, Gatan) was carried out in a JEOL 2010 TEM on commercial graphite powder (SP-1 graphite, Bay Carbon, Inc. Michigan, USA; the same graphite used to make the GO that was converted to MEGO), MEGO, and a-MEGO samples, respectively. High resolution SEM, STEM and EELS were performed using a dedicated STEM Hitachi HD2700C, equipped with a cold-field emission gun, a CEOS aberration corrector and a high-resolution (0.35eV) EELS Spectrometer (Gatan, Enfina). As noted in the main text, it was necessary to ignore the large percentage of the a-MEGO on the TEM grid, as it was too thick to perform EELS measurements on. We were successful in finding some thin, plate-shaped a-MEGO with a porous structure that was identical to that observed in the more three-dimensional chunks, shown in Figure 1C of the main text. It is possible to quantify the amount of sp<sup>2</sup>-bonding by measuring the ratio between  $\pi^*$  bonding and  $\pi^*+\delta^*$  bonding using EELS (3, 4). The relative amount of sp<sup>2</sup> carbon atoms was calculated by using the formula:

$$\frac{sp^2}{sp^2 + sp^3} = \frac{\frac{I_{\pi^*}^u}{I_{\pi^*}^u + I_{\sigma^*}^u}}{\frac{I_{\pi^*}^g}{I_{\pi^*}^g + I_{\sigma^*}^g}},$$

where the  $I^u$  and  $I^g$  represent the integrated intensity for specific energy ranges of the spectra for the a-MEGO and graphite (assumed to be 100% sp<sup>2</sup> carbon), respectively (3, 4). Comparisons were made between a-MEGO and graphite films of approximately the same thickness (as measured by comparing the intensity in the zero loss peak with the

intensity in the low-loss region) (5).  $I_{\pi^*}$  and  $I_{\sigma^*}$  are the peak intensities due to the  $1s \rightarrow \pi^*$  and  $1s \rightarrow \sigma^*$  transitions, corresponding to  $sp^2$  and  $sp^3$  hybridized carbon atoms. Two windows, 283.2-287.2 eV and 292.5-312.5 eV for the  $1s \rightarrow \pi^*$  and  $1s \rightarrow \sigma^*$  transitions, respectively, were integrated to generate the peak intensities. The resulting analyses reveal the fraction of  $sp^2$  bonding for the a-MEGO is  $98 \pm 2\%$ . The statistical error of 2% is consistent with the values expected using this approach (3). Complementary XPS measurements were also taken of the a-MEGO powder material with the Omicron Nanotechnology system (analyzer acceptance angle  $\pm 8^\circ$ , takeoff angle  $45^\circ$ , pass energy 15 eV) to establish the relative amount of  $sp^2$  carbon for comparison to the EELS measurements. The powder sample was supported on a surface that was nearly free of carbon and oxygen and that consisted of a Pt thin film that had been evaporated on a Si wafer. XPS data was analyzed using the CasaXPS fitting package and an asymmetric Doniach-Sunjić (DS) peak shape was used to fit the  $sp^2$  component, as required for conductive  $sp^2$  carbon materials (6, 7).

The powder conductivity of a-MEGO samples was obtained by the method described in Ref (1).

### 3. Supercapacitor measurements

A two-electrode cell configuration was used to measure the performance of supercapacitors with the a-MEGO and a-TEGO materials. 5 wt% Polytetrafluoroethylene (PTFE; 60 wt% dispersion in water) was added to the a-MEGO and a-TEGO as a binder. Typically, the a-MEGO (or a-TEGO) and PTFE was mixed into a paste using a mortar and pestle, rolled into uniform thickness sheets whose thickness ranged 40 to 50  $\mu\text{m}$  thick (from sheet to sheet) and punched into  $\sim 1\text{-cm}$  diameter electrodes. A pair of typical electrodes had a weight between 2.5 and 4.0 mg after drying overnight at a  $\sim 100^\circ\text{C}$  under vacuum. The two identical (by weight and size) electrodes were assembled in a test cell as shown in Ref (8), which consisted of two current collectors, two electrodes, and an ion-porous separator (Celgard<sup>®</sup> 3501) supported in a test fixture consisting of two stainless steel plates. Conductive carbon coated aluminum foils (Exopack<sup>™</sup> 0.5 mil 2-side coating) were used as current collectors. 1-butyl-3-methylimidazolium

tetrafluoroborate (BMIM BF<sub>4</sub>) was obtained commercially from Sigma Aldrich and diluted in acetonitrile (AN) with a weight ratio of 1:1 (with some testing done with neat BMIM BF<sub>4</sub>). The tetraethylammonium tetrafluoroborate (TEA BF<sub>4</sub>, Sigma Aldrich) was prepared at 1.0 M in AN. The 1-Ethyl-3-methylimidazolium bis(trifluoromethylsulfonyl)imide (EMIM TFSI, Sigma Aldrich) was used as purchased. The assembly of the test cell was done in a glove box filled with Ar.

Gravimetric capacitance from galvanostatic charge/discharge was calculated by using the formula

$$C_{carbon} = \frac{4I_{cons}}{m dV / dt},$$

where  $I$  is the constant current and  $m$  the total mass for both carbon electrodes, and  $dV/dt$  was calculated from the slope obtained by fitting a straight line to the discharge curve over the range of  $V_{max}$  (the voltage at the beginning of discharge) to  $\frac{1}{2} V_{max}$ . Based on a RC model, the capacitance was also calculated from the frequency response analysis, by  $C = -1/(2\pi f Z'')$ , where  $f$  is frequency in Hz and  $Z''$  is the imaginary part of the impedance, to show the trend of changes in capacitance with frequency. The energy density was estimated by using the formula  $E_{cell} = CV_{max}^2/8$ , where the cell mass (two carbon electrodes) was normalized. Effective series resistance (ESR) was estimated using the voltage drop at the beginning of the discharge,  $V_{drop}$ , at certain constant current  $I_{cons}$ , with the formula  $R_{ESR} = V_{drop}/(2I_{cons})$ . The power density, calculated from the discharge data at certain constant current  $I_{cons}$ , and normalized with the weight of the carbon cell (two carbon electrodes) is given by

$$P = \frac{(V_{max} - V_{drop})^2}{4R_{ESR}m}.$$



#### 4. Dependence of a-MEGO SSA on ratio of KOH to MEGO

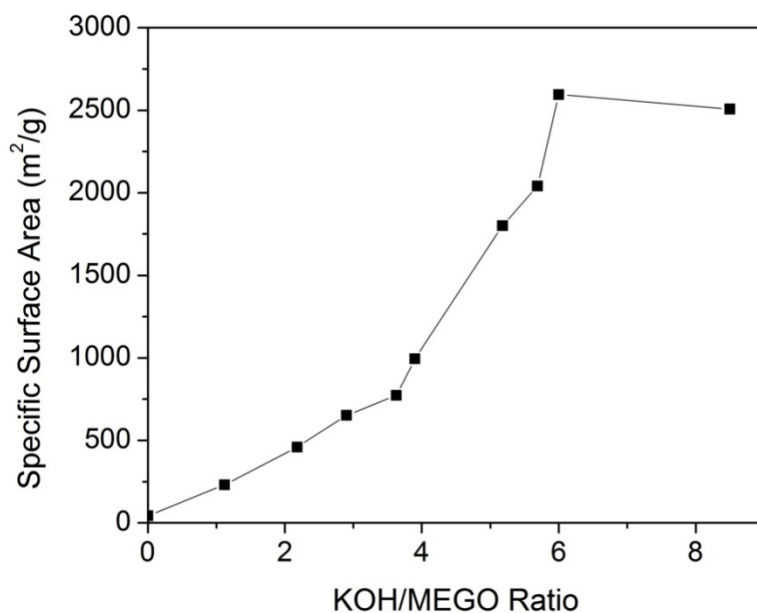


Fig. S1 The BET specific surface area (SSA) of a-MEGO versus the KOH to MEGO loading ratio in the mixture before activation. For this series of samples, the highest SSA was about 2600 m<sup>2</sup>/g.

## 5. SEM/STEM images of a-MEGO

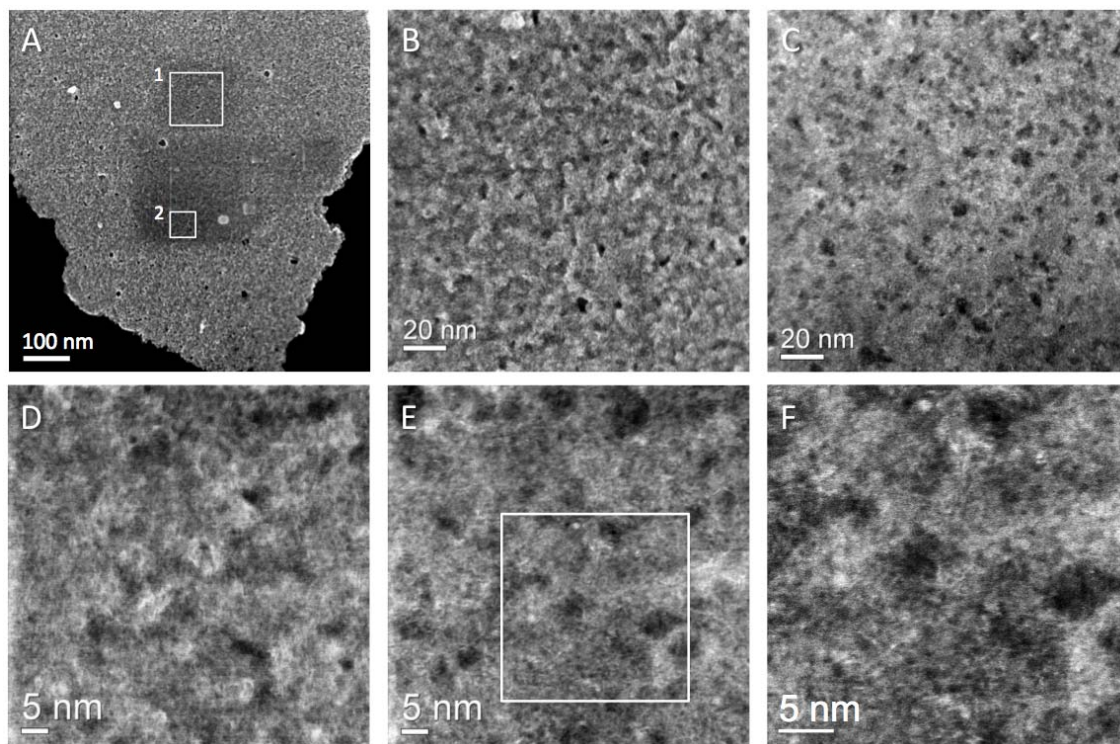


Fig. S2 (A) Low magnification SEM and (B) high magnification SEM and (C) ADF-STEM images of a-MEGO. (B and C) are simultaneously taken from the region 1 in (A). Larger pores of between 2-10 nm are clearly resolved. (D) Very high magnification SEM and (E) ADF-STEM images simultaneously taken from the region 2 in (A), with (F) being from the region outlined as a box in (E). These images indicate that the entire microstructure is composed of very small pores, of order of  $\sim 1$  nm in size, as is evident in the magnified portion shown as (F).

## 6. EPR measurements of a-MEGO

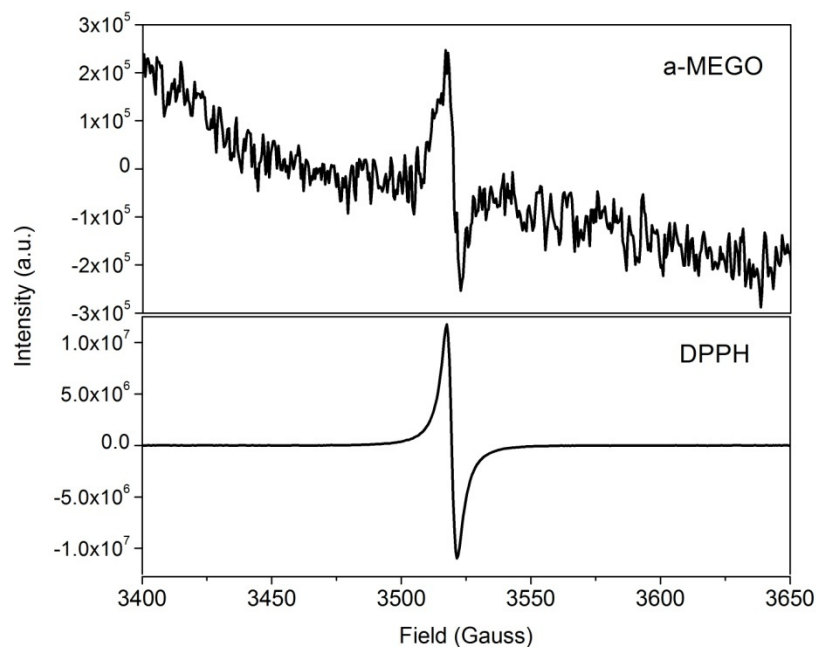


Fig. S3 EPR data of a-MEGO with DPPH used as a standard. Samples of a-MEGO (SSA  $\sim 2520 \text{ m}^2/\text{g}$ ), and of DPPH diluted in KCl, were measured in 4 mm tubes under similar conditions except for the number of scans. 400 scans were run on a-MEGO to obtain sufficient signal/noise ratio; only 40 scans were run on DPPH to avoid saturation. Double integrated areas of as-measured curves were normalized with the number of scans and mass of each sample. A concentration of  $\sim 2 \times 10^{16}$  spins/g was estimated for this a-MEGO sample, corresponding to a concentration of 0.4 spins per million carbon atoms.

## 7. XPS data for a-MEGO and analysis

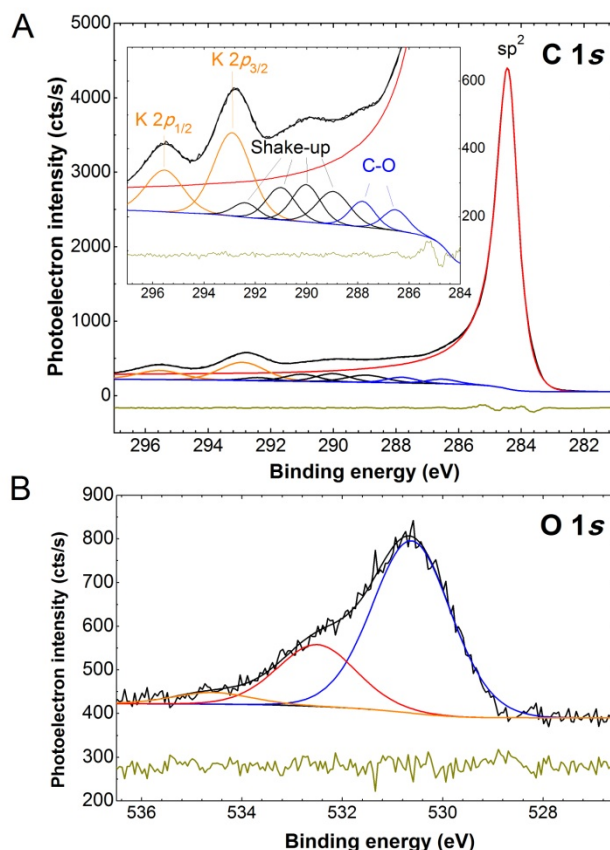


Fig. S4 Detailed XPS analysis of a-MEGO sample (SSA  $\sim 2520 \text{ m}^2/\text{g}$ ). (A) Fit to the C 1s region is shown, with detailed spectrum inset. The main  $sp^2$  carbon peak is a Doniach-Sunjić line with asymmetry parameter  $\alpha=0.20$  and FWHM 0.78 eV, which are reasonably close to values for these parameters in fits to highly oriented pyrolytic graphite (HOPG) and glassy carbon (7). Multiple states are also present on the high binding energy side of the main  $sp^2$  peak. An  $sp^3$  component, if present, is expected at +0.8 to +0.9 eV above the  $sp^2$  component in the C 1s spectrum (9). Attempts to fit the spectral envelope with an  $sp^3$  component indicate that  $sp^3$  carbon is below the limit of detection of XPS (approximately 1 at. %). Two C 1s states are observed at +2.0 and +3.3 eV above the main  $sp^2$  peak (with widths of 1.2 eV) and are attributed to C-O bonding with corresponding states observed in the O 1s and impurity K 2p spectra. Several shake-up features are also present at +4.4, +5.5, +6.5 and +7.9 eV above the main  $sp^2$  peak (widths of 1.5, 1.3, 1.3 and 1.1 eV



respectively) and are in good agreement with fits to the extended shake-up energy loss spectrum of glassy carbon and highly oriented pyrolytic graphite (HOPG) by Leiro et. al.(7). Residual potassium (< 2 at. %) from the KOH activation process is detected as a K  $2p$  doublet with the K  $2p_{3/2}$  state observed at 292.9 eV. (B) The O  $1s$  region is shown and composed of three components at 530.6 eV ( $K_2CO_3$ ), 532.5 eV ( $KHCO_3$ ) and 534.6 eV (KOH) (10-12). It is noted that the C  $1s$  shake up features described above make the unequivocal deconvolution of a carbonate bond problematic. Residual peak fitting error is shown beneath all spectra.

## 8. Raman and FTIR analysis of a-MEGO

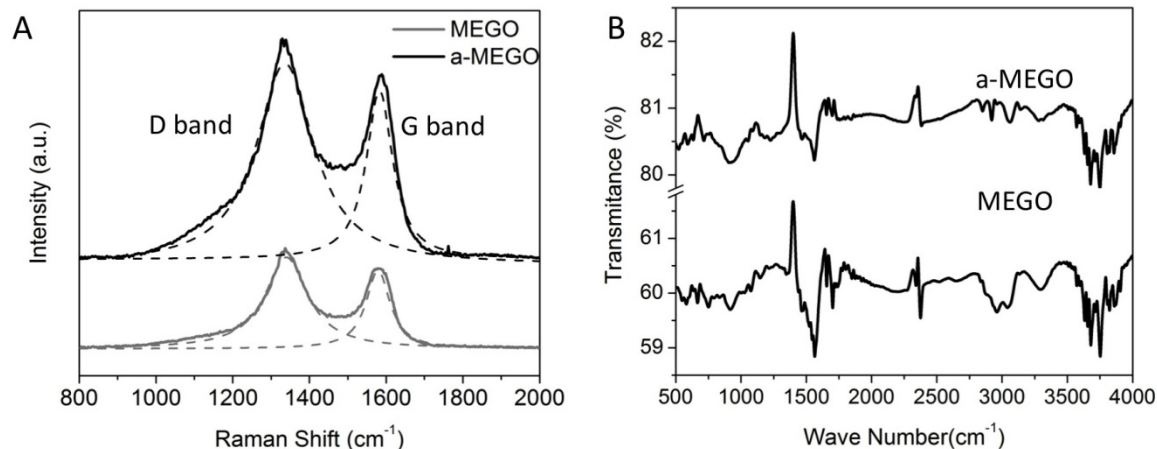


Fig. S5 (A) Raman of a-MEGO and MEGO control sample. The  $I_d/I_g$  slightly increases from  $\sim 1.16$  in MEGO to  $\sim 1.19$  in a-MEGO. From Lorentzian fitting, the D band FWHM increases from  $\sim 135$  to  $\sim 183$  cm<sup>-1</sup>. (B) FTIR transmittance spectra. The following bands were observed: O-H stretching (3200-3400 cm<sup>-1</sup>), C-H aliphatic (2800-3000 cm<sup>-1</sup>), C=O and C-O stretching (1640-1750 cm<sup>-1</sup>), aromatic C=C stretching (1400-1600 cm<sup>-1</sup>) and bands related to aromatic content (700-920 cm<sup>-1</sup>) such as out of plane C-H bending ( $\sim 910$  cm<sup>-1</sup>) with different degrees of substitution. Compared with the MEGO control sample, a-MEGO shows lower signals from the oxygen or hydrogen containing groups.

## 9. Comparison of N<sub>2</sub> BET data for MEGO and a-MEGO

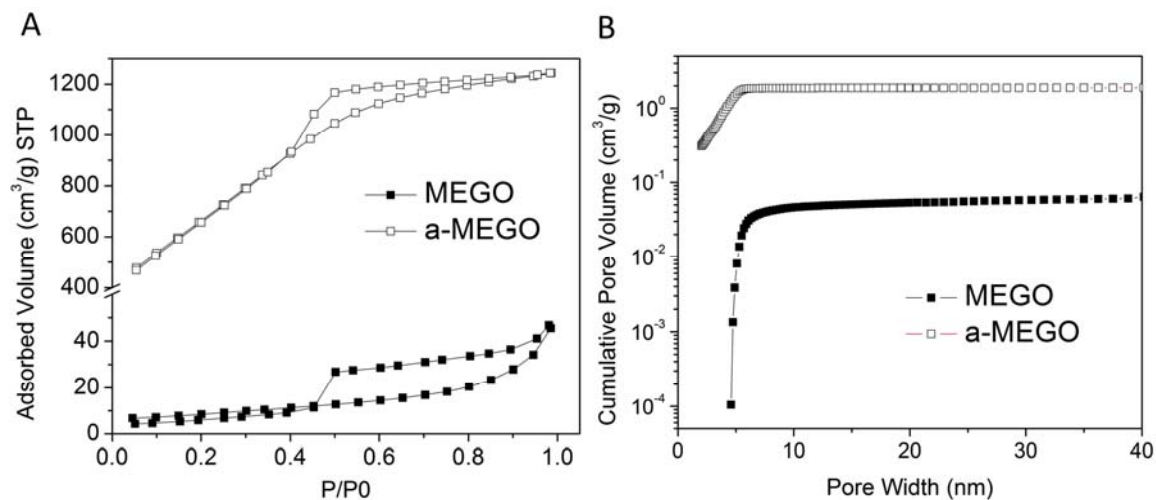


Fig. S6 N<sub>2</sub> adsorption/desorption analysis of a-MEGO ( $\sim 2520 \text{ m}^2/\text{g}$ ) with MEGO as control. (A) N<sub>2</sub> isotherm curves at 77.4 K. (B) Cumulative pore volume versus pore diameter plots obtained from the adsorption isotherm in (A). NLDFIT analysis for carbon with slit/cylindrical model was used on the adsorption data to obtain the pore volumes.

## 10. QSDFT pore size distribution of a-MEGO

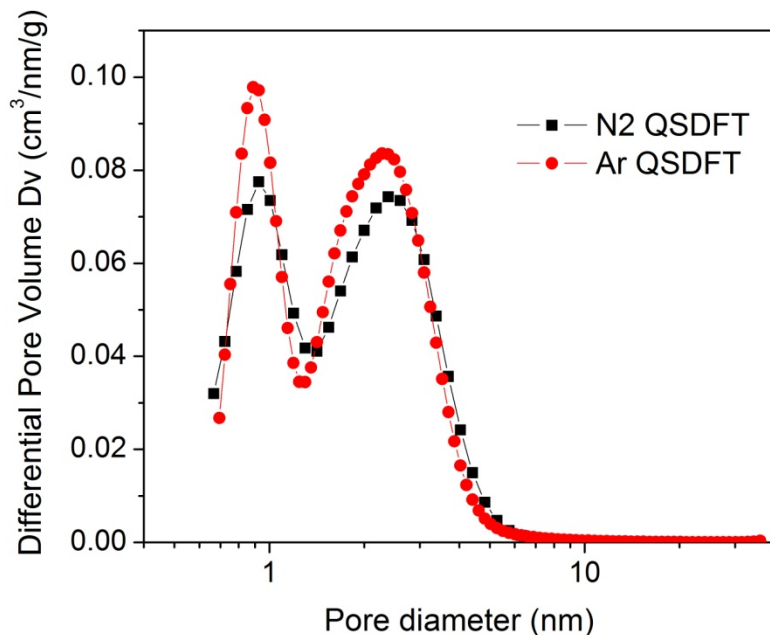


Fig S7 ‘Quenched solid density functional theory’ (QSDFT) pore size distribution of a-MEGO. In addition to the NLDFT pore size distribution shown in Fig. 3B (which was based on NLDFT assuming a slit/cylindrical pore hybrid model), we also analyzed the nitrogen (77.4 K) and argon (87.3 K) adsorption isotherms by assuming a slit pore model and QSDFT, which quantitatively accounts for the surface geometrical inhomogeneity. It follows that this pore size distribution essentially resembles the distribution from the slit/cylindrical pore model shown in the manuscript (Fig. 3 B); however, the mesopore size is slightly smaller in the slit pore QSDFT model.



## 11. Supercapacitor performance of a-MEGO with TEA BF<sub>4</sub>/AN electrolyte

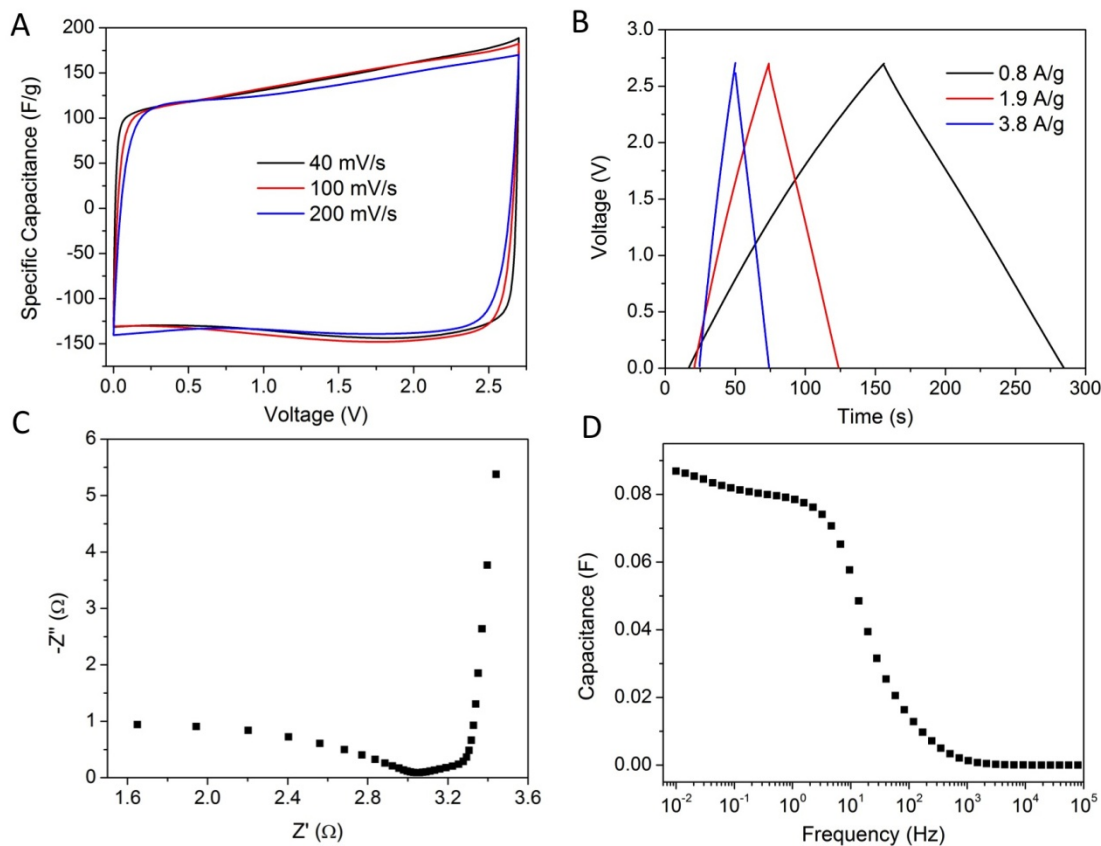


Fig. S8 Supercapacitor performance of a-MEGO (SSA  $\sim 3100 \text{ m}^2/\text{g}$ ) with 1.0 M TEA BF<sub>4</sub>/AN electrolyte. (A) CV curves for different scan rates. Rectangular shapes indicate the capacitive behavior. (B) Galvanostatic charge/discharge curves of a-MEGO based supercapacitor under different constant currents. The specific capacitances calculated from the discharge curves are 154, 145 and 141 F/g, for the constant currents of 0.8, 1.9 and 3.8 A/g, respectively. From the discharge data obtained at the constant current of 0.8 A/g, the energy density and power density were estimated as 39 Wh/kg and 145 kW/kg, respectively, when normalized with the total weight of two a-MEGO electrodes. (C) Nyquist plot, displaying a similar resistance as that of a-MEGO in BMIM BF<sub>4</sub>/AN electrolyte. (D) Frequency response of the capacitance of the a-MEGO supercapacitor.

## 12. Stability testing of supercapacitor having a-MEGO with BMIM BF<sub>4</sub> electrolyte

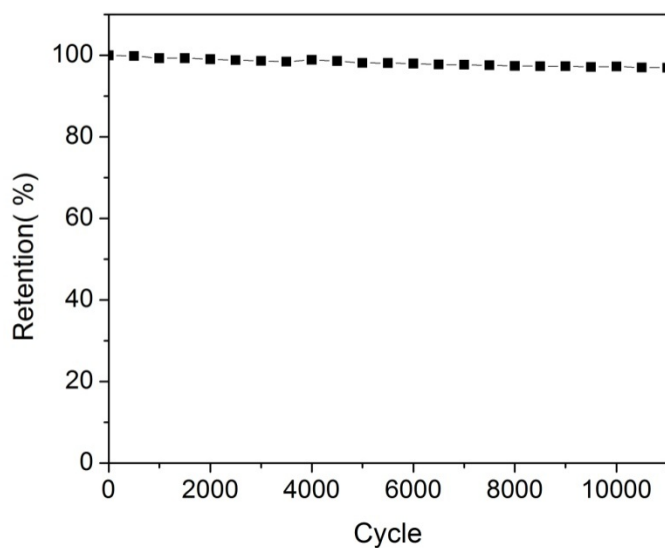


Fig. S9 Testing of the a-MEGO (with surface area of  $\sim 3100 \text{ m}^2/\text{g}$ ) based supercapacitor in neat BMIM BF<sub>4</sub> over 10000 cycles. Constant current cycles were run at a rate of 2.5 A/g. Retention of 97% was obtained after 10000 cycles. Here the pure IL was used as electrolyte to minimize possible contamination.

### 13. Supercapacitor performance of a-MEGO with EMIM TFSI electrolyte

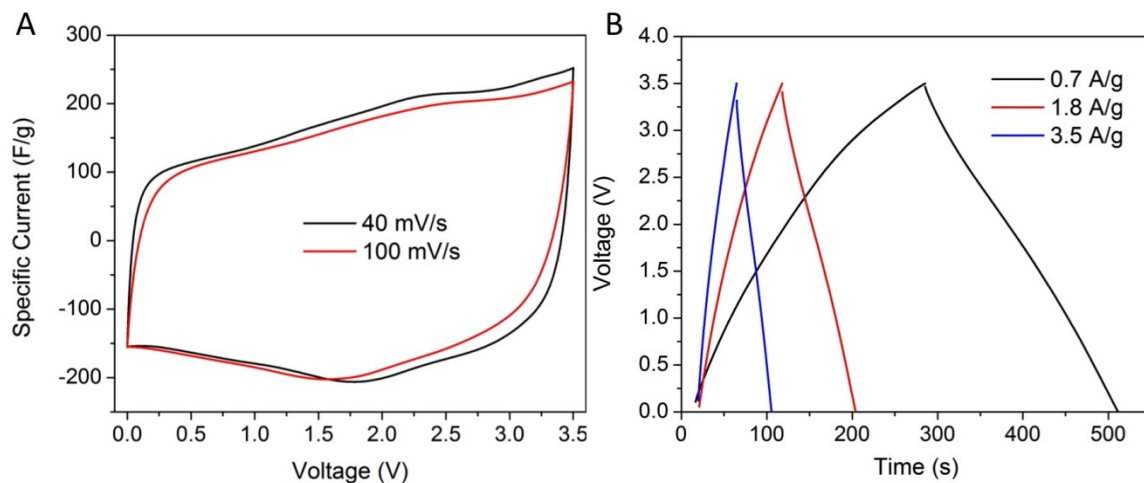


Fig. S10 Supercapacitor performance of a-MEGO (SSA  $\sim 3100 \text{ m}^2/\text{g}$ ) in neat EMIM TFSI electrolyte. (A) CV curves under different scan rates. (B) Galvanostatic charge/discharge curves under different constant currents. The specific capacitances calculated from the discharge curves with maximum voltage of 3.5 V are 200, 192 and 187 F/g for the currents of 0.7, 1.8 and 3.5 A/g, respectively. The normalized ESR is  $0.025 \Omega \cdot \text{g}$ . From the discharge data obtained at the constant current of 0.7 A/g, the energy density and power density were estimated as 85 Wh/kg and 122 kW/kg, when normalized with the total weight of the two a-MEGO electrodes.

#### 14. N<sub>2</sub> adsorption results of a-TEGO

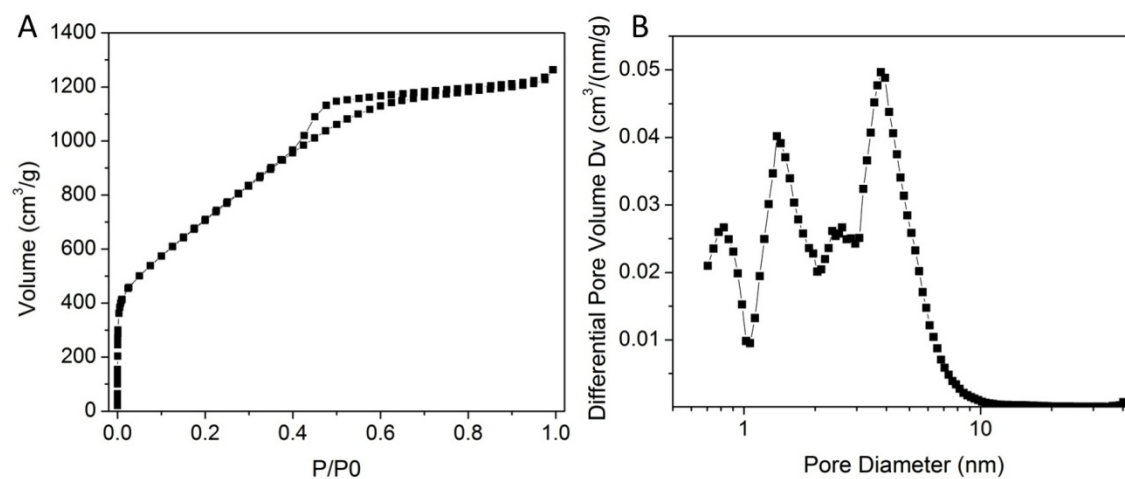


Fig. S11 N<sub>2</sub> adsorption/desorption analysis of a-TEGO. (A) High resolution, low pressure isotherm, from which a high BET SSA of 2675 m<sup>2</sup>/g (calculated in the linear relative pressure range from 0.1 to 0.3) is obtained. (B) Pore size distribution for N<sub>2</sub> adsorption (calculated using a slit/cylindrical NLDFT model).

## 15. Supercapacitor performance of a-TEGO with BMIM BF<sub>4</sub>/AN electrolyte

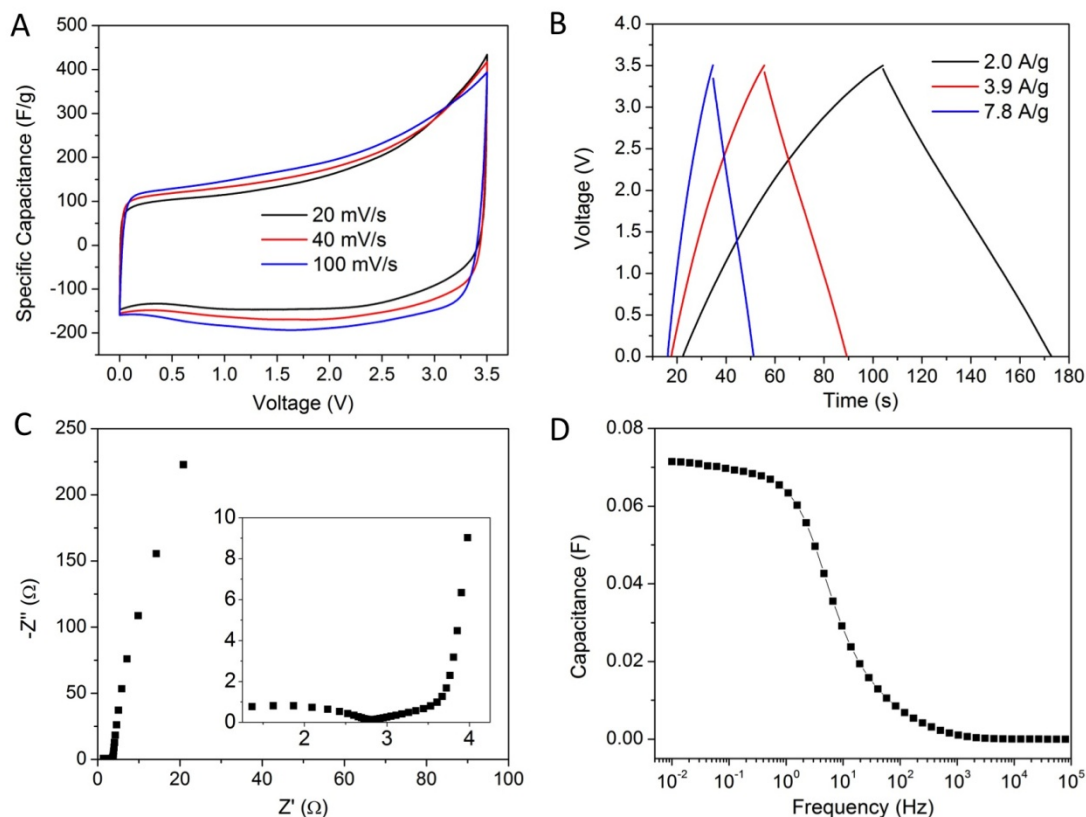


Fig. S12 Supercapacitor performance of a-TEGO (SSA  $\sim 2700 \text{ m}^2/\text{g}$ ) in the BMIM BF<sub>4</sub>/AN electrolyte. (A) CV curves for different scan rates. (B) Galvanostatic charge/discharge curves under different constant currents. The capacitance values calculated are 156, 154 and 154 F/g for the currents of 2.0, 3.9 and 7.8 A/g, respectively. From the discharge data obtained at the constant current of 2.0 A/g, the ESR, energy density and power density were estimated as 4.1  $\Omega$ , 66 Wh/kg and 282 kW/kg, respectively. (C) Nyquist plot for the a-TEGO based supercapacitor. (D) Frequency response of the capacitance of the a-TEGO supercapacitor in BMIM BF<sub>4</sub>/AN electrolyte.

## 16. Movies S1

Movies S1 Through-focal series high resolution TEM images of the a-MEGO structure. The images were obtained at 80 kV on the aberration corrected FEI Titan, with a focal step of  $-4$  nm per image. Initial focus is deliberately slightly over-focus, and scans through slightly under-focus, so that in a given frame some portion of the wedge-shaped sample is in exact / Scherzer defocus. The images show that the a-MEGO structure is composed of a high density of pores of very small size, with the pore walls being composed of single carbon sheets.

## 17. References

1. Y. Zhu *et al.*, *Carbon* **48**, 2118 (2010).
2. H. C. Schniepp *et al.*, *Journal of Physical Chemistry B* **110**, 8535 (2006).
3. S. D. Berger, D. R. McKenzie, P. J. Martin, *Philosophical Magazine Letters* **57**, 285 (1988).
4. H. Daniels, R. Brydson, B. Rand, A. Brown, *Philosophical Magazine* **87**, 4073 (2007).
5. R. Egerton, *Electron energy loss spectroscopy in the electron microscope*. (Plenum, New York, ed. 2nd, 1996).
6. S. Doniach, M. Sunjic, *Journal of Physics C: Solid State Physics* **3**, 285 (1970).
7. J. A. Leiro, M. H. Heinonen, T. Laiho, I. G. Batirev, *Journal of Electron Spectroscopy and Related Phenomena* **128**, 205 (2003).
8. M. D. Stoller, R. S. Ruoff, *Energy & Environmental Science* **3**, 1294 (2010).
9. R. Haerle, E. Riedo, A. Pasquarello, A. Baldereschi, *Physical Review B* **65**, 045101 (2001).
10. A. Shchukarev, D. Korolkov, *Central European Journal of Chemistry* **2**, 347 (2004).
11. P. M. Blass, X. L. Zhou, J. M. White, *The Journal of Physical Chemistry* **94**, 3054 (1990).
12. D. V. Chakarov, *et al.*, *Journal of Physics: Condensed Matter* **5**, 2903 (1993).





[www.sciencemag.org/cgi/content/full/science.1200770/DC1](http://www.sciencemag.org/cgi/content/full/science.1200770/DC1)

Supporting Online Material for

## **Carbon-Based Supercapacitors Produced by Activation of Graphene**

Yanwu Zhu, Shanthi Murali, Meryl D. Stoller, K. J. Ganesh, Weiwei Cai, Paulo J. Ferreira, Adam Pirkle, Robert M. Wallace, Katie A. Cychosz, Matthias Thommes, Dong Su, Eric A. Stach, Rodney S. Ruoff\*

\*To whom correspondence should be addressed. E-mail: [r.ruoff@mail.utexas.edu](mailto:r.ruoff@mail.utexas.edu)

Published 12 May 2011 on *Science Express*  
DOI: 10.1126/science.1200770

### **This PDF file includes:**

SOM Text

Figs. S1 to S12

References

**Other Supporting Online Material for this manuscript includes the following:**  
(available at [www.sciencemag.org/cgi/content/full/science.1200770/DC1](http://www.sciencemag.org/cgi/content/full/science.1200770/DC1))

Movie S1

Supporting Online Materials for

## **Carbon-based Supercapacitors Produced by Activation of Graphene**

Yanwu Zhu,<sup>1</sup> Shanthi Murali,<sup>1</sup> Meryl D. Stoller,<sup>1</sup> K. J. Ganesh,<sup>1</sup> Weiwei Cai,<sup>1</sup>  
Paulo J. Ferreira,<sup>1</sup> Adam Pirkle,<sup>2</sup> Robert M. Wallace,<sup>2</sup> Katie A. Cychosz,<sup>3</sup> Matthias  
Thommes,<sup>3</sup> Dong Su,<sup>4</sup> Eric A. Stach,<sup>4</sup> Rodney S. Ruoff<sup>1,\*</sup>

<sup>1</sup>Department of Mechanical Engineering and Materials Science and Engineering Program, The  
University of Texas at Austin, One University Station C2200, Austin, TX 78712

<sup>2</sup>Department of Materials Science and Engineering, The University of Texas at Dallas, 800 W.  
Campbell Rd, Richardson, TX 75080

<sup>3</sup>Quantachrome Instruments, 1900 Corporate Drive, Boynton Beach, FL 33426

<sup>4</sup>Center for Functional Nanomaterials, Brookhaven National Laboratory, Upton, NY 11973

\*E-mail: [r.ruoff@mail.utexas.edu](mailto:r.ruoff@mail.utexas.edu)

### **Table of Contents**

- 1. Synthesis of a-MEGO and a-TEGO from MEGO and TEGO**
- 2. Characterization methods**
- 3. Supercapacitor measurements**
- 4. Fig. S1: dependence of a-MEGO SSA on ratio of KOH to MEGO**
- 5. Fig. S2: SEM/STEM images of a-MEGO**
- 6. Fig. S3: EPR measurements of a-MEGO**
- 7. Fig. S4: XPS data for a-MEGO and analysis**
- 8. Fig. S5: Raman and FTIR analysis of a-MEGO**
- 9. Fig. S6: Comparison of N<sub>2</sub> BET data for MEGO and a-MEGO**
- 10. Fig. S7: QSDFT pore size distribution of a-MEGO**
- 11. Fig. S8: Supercapacitor performance of a-MEGO with TEA BF<sub>4</sub>/AN electrolyte**
- 12. Fig. S9: Stability testing of supercapacitor having a-MEGO with BMIM BF<sub>4</sub> electrolyte**
- 13. Fig. S10: Supercapacitor performance of a-MEGO with EMIM TFSI electrolyte**
- 14. Fig. S11: N<sub>2</sub> adsorption results for a-TEGO**
- 15. Fig. S12: Supercapacitor performance of a-TEGO with BMIM BF<sub>4</sub>/AN electrolyte**
- 16. Movies S1**
- 17. References**

## 1. Synthesis of a-MEGO and a-TEGO from MEGO and TEGO

The synthesis of microwave exfoliated graphite oxide (MEGO) followed the method described in Ref (1). Briefly, graphite oxide (GO) powders made from the modified Hummers' method were irradiated in a domestic microwave oven (GE, JES0736SM1SS) operated at 1100 W for 1 minute. During the irradiation, a large volume expansion of the GO powder occurred and the black, fluffy MEGO powder obtained was collected for activation. Typically, 400 mg MEGO powder was dispersed in 20 ml 7M aqueous KOH solution and stirred for 4 hours at a speed of 400 rpm, followed by another 20 hours of static soaking in ambient conditions. The extra KOH solution was removed by briefly filtering the mixture through a polycarbonate membrane (Whatman, 0.2  $\mu\text{m}$ ); then the mixture was dried in the lab environment at 65 °C for 24 hours. A control MEGO sample, made with the same soaking-drying process but with no KOH was also prepared, and 85% of the mass remained after drying. A KOH to MEGO ratio was calculated by assuming the MEGO in the dry MEGO/KOH mixture gave the same mass yield, i.e., 85%.

It was found that the KOH uptake (KOH/MEGO ratio) was linearly dependent on the molarity of the KOH solution, with other process parameters held constant (such as the amount of MEGO from the same batch of GO and the volume of KOH solution). For the MEGO soaked in 20 ml 7M KOH as described above, the KOH/MEGO ratio was  $8.9 \pm 0.3$ . The dry MEGO/KOH mixture was heated at 800 °C for 1 hour in a horizontal tube furnace (50-mm diameter), with an argon flow of 150 sccm and working pressure of  $\sim 400$  Torr. The temperature was ramped from room temperature to 800 °C at 5 °C/min. After cooling down in vacuum, the sample was repeatedly washed by de-ionized water until a pH value of 7 was reached. Then the sample was dried at 65 °C in ambient for 2 hours, followed by thermal annealing at 800 °C in vacuum (0.1 Torr) for 2 hours, to generate 'activated MEGO' (a-MEGO) powders. Thermally exfoliated graphite oxide ('TEGO'), made by 'thermal shocking' of GO at 250 °C in ambient (2), was activated following the same process. The a-MEGO and a-TEGO so obtained were characterized in a variety of ways, and supercapacitor measurements were made, as described in the main text and below.

## 2. Characterization methods

The a-MEGO was analyzed by scanning electron microscopy (SEM, Hitachi S5500, 30 kV), transmission electron microscopy (TEM, JEOL 2010F, 200 kV at UT-Austin; TEM, spherical aberration corrected FEI Titan 80/300, 80 kV at BNL; the spherical and chromatic aberration corrected TEAM instrument at LBNL, see: [ncem.lbl.gov/TEAM-project/](http://ncem.lbl.gov/TEAM-project/)) and scanning TEM (Aberration corrected Hitachi HD2700C at BNL). The exit wave reconstructed image shown in Figure 1F was processed using the MacTempas Exit Wave Reconstruction Package ([totalresolution.com](http://totalresolution.com)) from a series of 41 images, ranging from 28 nm above Gaussian to 28 nm below Gaussian and with 1.4 nm focal step size.

The measurement of the nitrogen adsorption isotherms was done with a Quantachrome Nova 2000 at 77.4 K to obtain the surface areas of a-MEGO samples from different KOH/MEGO ratios, and for the comparison between MEGO control and a-MEGO samples. Detailed adsorption experiments with nitrogen (77.4K), argon (87.3 K), and carbon dioxide (273.2 K) were also performed with a Quantachrome Autosorb iQ MP in order to assess surface area and pore characteristics of the a-MEGO. Nitrogen adsorption with the Quantachrome Autosorb iQ MP was also carried out on the a-TEGO. The samples were outgassed at 150 °C for 16 hours under turbomolecular vacuum pumping prior to the gas adsorption measurements.

Samples were sealed into glass Lindemann capillaries and x-ray diffraction patterns collected at the X12A beamline of the National Synchrotron Light Source, using x-rays of 0.699 Angstrom wavelength, in parallel beam geometry. Background from the glass was normalized at high angles, and the data converted to Cu K  $\alpha$  for the plot shown in Fig. 2A.

Micro Raman was done on a Witec Alpha 300 confocal Raman system with a laser wavelength of 532 nm. Lorentzian fitting was done to obtain the positions and widths of the D and G bands in the Raman shift spectra. Fourier transform infrared spectroscopy (FTIR) was done with a Perkin Elmer Spectrum BX.

X-ray photoelectron spectroscopy (XPS) was conducted with two separate systems equipped with monochromatic Al K $\alpha$  sources (Kratos AXIS Ultra DLD, Omicron Nanotechnology XM1000/EA 125 U7) to analyze the chemical composition of the samples.

Combustion elemental analysis was done at Atlantic Microlab, Inc. (Georgia, USA) for determination of the C, O, and H content. Electron paramagnetic resonance (EPR) measurements of a-MEGO were done with a Bruker EMX Plus (X band, 295 K) with 2,2-Di(4-tert-octylphenyl)-1-picrylhydrazyl (DPPH, Sigma Aldrich 257612) as a standard.

Electron energy loss spectroscopy (EELS, Gatan) was carried out in a JEOL 2010 TEM on commercial graphite powder (SP-1 graphite, Bay Carbon, Inc. Michigan, USA; the same graphite used to make the GO that was converted to MEGO), MEGO, and a-MEGO samples, respectively. High resolution SEM, STEM and EELS were performed using a dedicated STEM Hitachi HD2700C, equipped with a cold-field emission gun, a CEOS aberration corrector and a high-resolution (0.35eV) EELS Spectrometer (Gatan, Enfina). As noted in the main text, it was necessary to ignore the large percentage of the a-MEGO on the TEM grid, as it was too thick to perform EELS measurements on. We were successful in finding some thin, plate-shaped a-MEGO with a porous structure that was identical to that observed in the more three-dimensional chunks, shown in Figure 1C of the main text. It is possible to quantify the amount of sp<sup>2</sup>-bonding by measuring the ratio between  $\pi^*$  bonding and  $\pi^*+\delta^*$  bonding using EELS (3, 4). The relative amount of sp<sup>2</sup> carbon atoms was calculated by using the formula:

$$\frac{sp^2}{sp^2 + sp^3} = \frac{\frac{I_{\pi^*}^u}{I_{\pi^*}^u + I_{\sigma^*}^u}}{\frac{I_{\pi^*}^g}{I_{\pi^*}^g + I_{\sigma^*}^g}},$$

where the  $I^u$  and  $I^g$  represent the integrated intensity for specific energy ranges of the spectra for the a-MEGO and graphite (assumed to be 100% sp<sup>2</sup> carbon), respectively (3, 4). Comparisons were made between a-MEGO and graphite films of approximately the same thickness (as measured by comparing the intensity in the zero loss peak with the

intensity in the low-loss region) (5).  $I_{\pi^*}$  and  $I_{\sigma^*}$  are the peak intensities due to the  $1s \rightarrow \pi^*$  and  $1s \rightarrow \sigma^*$  transitions, corresponding to  $sp^2$  and  $sp^3$  hybridized carbon atoms. Two windows, 283.2-287.2 eV and 292.5-312.5 eV for the  $1s \rightarrow \pi^*$  and  $1s \rightarrow \sigma^*$  transitions, respectively, were integrated to generate the peak intensities. The resulting analyses reveal the fraction of  $sp^2$  bonding for the a-MEGO is  $98 \pm 2\%$ . The statistical error of 2% is consistent with the values expected using this approach (3). Complementary XPS measurements were also taken of the a-MEGO powder material with the Omicron Nanotechnology system (analyzer acceptance angle  $\pm 8^\circ$ , takeoff angle  $45^\circ$ , pass energy 15 eV) to establish the relative amount of  $sp^2$  carbon for comparison to the EELS measurements. The powder sample was supported on a surface that was nearly free of carbon and oxygen and that consisted of a Pt thin film that had been evaporated on a Si wafer. XPS data was analyzed using the CasaXPS fitting package and an asymmetric Doniach-Sunjić (DS) peak shape was used to fit the  $sp^2$  component, as required for conductive  $sp^2$  carbon materials (6, 7).

The powder conductivity of a-MEGO samples was obtained by the method described in Ref (1).

### 3. Supercapacitor measurements

A two-electrode cell configuration was used to measure the performance of supercapacitors with the a-MEGO and a-TEGO materials. 5 wt% Polytetrafluoroethylene (PTFE; 60 wt% dispersion in water) was added to the a-MEGO and a-TEGO as a binder. Typically, the a-MEGO (or a-TEGO) and PTFE was mixed into a paste using a mortar and pestle, rolled into uniform thickness sheets whose thickness ranged 40 to 50  $\mu\text{m}$  thick (from sheet to sheet) and punched into  $\sim 1\text{-cm}$  diameter electrodes. A pair of typical electrodes had a weight between 2.5 and 4.0 mg after drying overnight at a  $\sim 100^\circ\text{C}$  under vacuum. The two identical (by weight and size) electrodes were assembled in a test cell as shown in Ref (8), which consisted of two current collectors, two electrodes, and an ion-porous separator (Celgard<sup>®</sup> 3501) supported in a test fixture consisting of two stainless steel plates. Conductive carbon coated aluminum foils (Exopack<sup>™</sup> 0.5 mil 2-side coating) were used as current collectors. 1-butyl-3-methylimidazolium

tetrafluoroborate (BMIM BF<sub>4</sub>) was obtained commercially from Sigma Aldrich and diluted in acetonitrile (AN) with a weight ratio of 1:1 (with some testing done with neat BMIM BF<sub>4</sub>). The tetraethylammonium tetrafluoroborate (TEA BF<sub>4</sub>, Sigma Aldrich) was prepared at 1.0 M in AN. The 1-Ethyl-3-methylimidazolium bis(trifluoromethylsulfonyl)imide (EMIM TFSI, Sigma Aldrich) was used as purchased. The assembly of the test cell was done in a glove box filled with Ar.

Gravimetric capacitance from galvanostatic charge/discharge was calculated by using the formula

$$C_{carbon} = \frac{4I_{cons}}{m dV / dt},$$

where  $I$  is the constant current and  $m$  the total mass for both carbon electrodes, and  $dV/dt$  was calculated from the slope obtained by fitting a straight line to the discharge curve over the range of  $V_{max}$  (the voltage at the beginning of discharge) to  $\frac{1}{2} V_{max}$ . Based on a RC model, the capacitance was also calculated from the frequency response analysis, by  $C = -1/(2\pi f Z'')$ , where  $f$  is frequency in Hz and  $Z''$  is the imaginary part of the impedance, to show the trend of changes in capacitance with frequency. The energy density was estimated by using the formula  $E_{cell} = CV_{max}^2/8$ , where the cell mass (two carbon electrodes) was normalized. Effective series resistance (ESR) was estimated using the voltage drop at the beginning of the discharge,  $V_{drop}$ , at certain constant current  $I_{cons}$ , with the formula  $R_{ESR} = V_{drop}/(2I_{cons})$ . The power density, calculated from the discharge data at certain constant current  $I_{cons}$ , and normalized with the weight of the carbon cell (two carbon electrodes) is given by

$$P = \frac{(V_{max} - V_{drop})^2}{4R_{ESR}m}.$$



#### 4. Dependence of a-MEGO SSA on ratio of KOH to MEGO

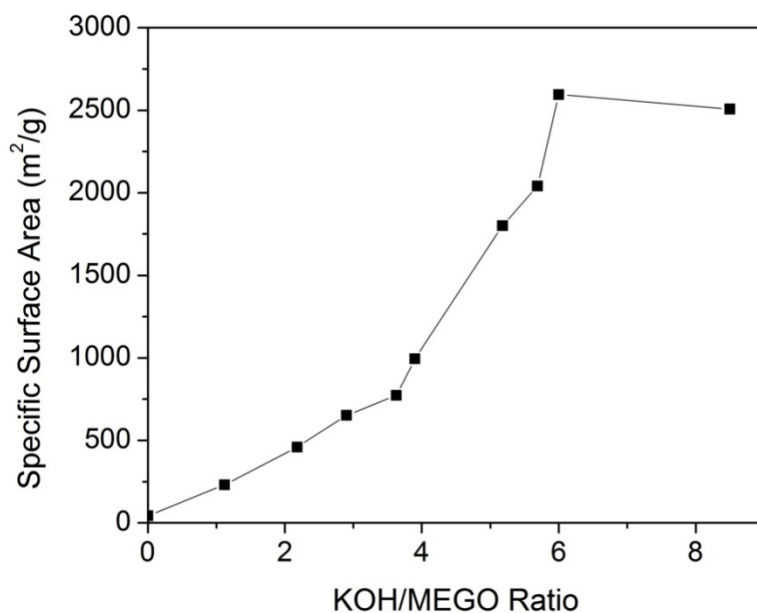


Fig. S1 The BET specific surface area (SSA) of a-MEGO versus the KOH to MEGO loading ratio in the mixture before activation. For this series of samples, the highest SSA was about 2600 m<sup>2</sup>/g.

## 5. SEM/STEM images of a-MEGO

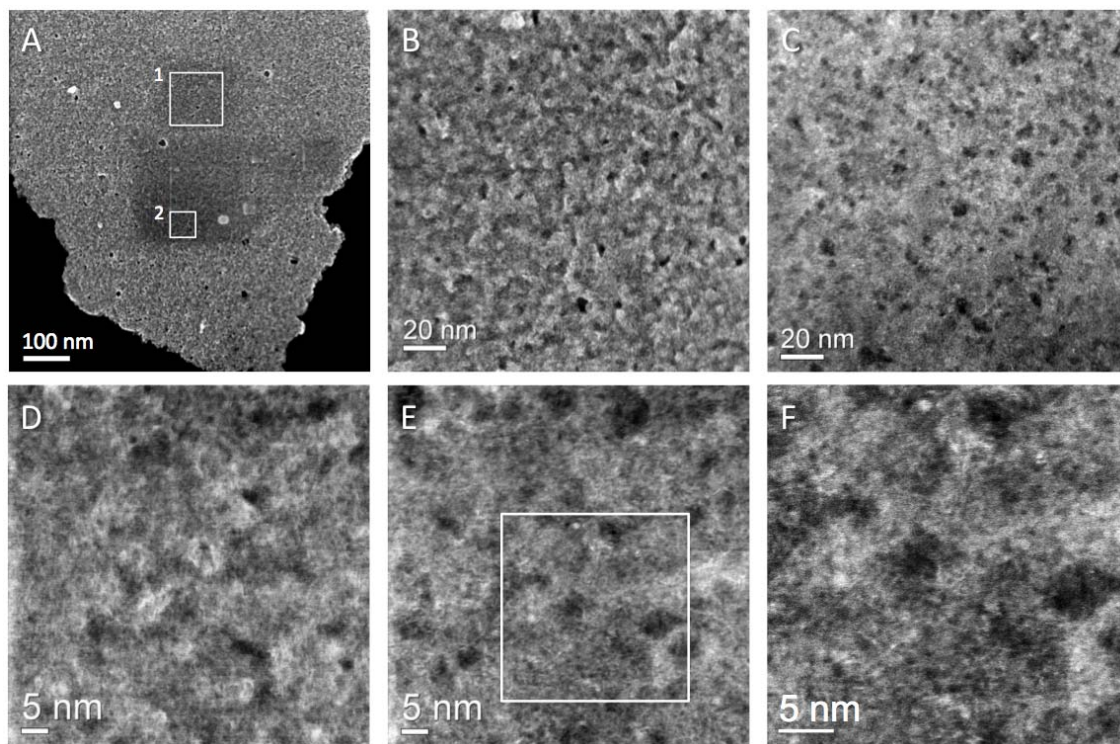


Fig. S2 (A) Low magnification SEM and (B) high magnification SEM and (C) ADF-STEM images of a-MEGO. (B and C) are simultaneously taken from the region 1 in (A). Larger pores of between 2-10 nm are clearly resolved. (D) Very high magnification SEM and (E) ADF-STEM images simultaneously taken from the region 2 in (A), with (F) being from the region outlined as a box in (E). These images indicate that the entire microstructure is composed of very small pores, of order of  $\sim 1$  nm in size, as is evident in the magnified portion shown as (F).

## 6. EPR measurements of a-MEGO

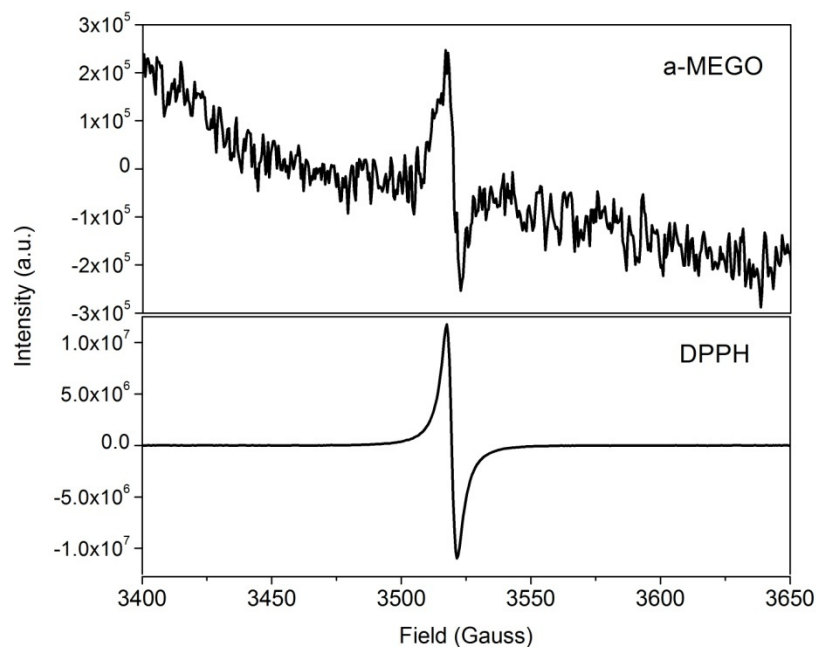


Fig. S3 EPR data of a-MEGO with DPPH used as a standard. Samples of a-MEGO (SSA  $\sim 2520 \text{ m}^2/\text{g}$ ), and of DPPH diluted in KCl, were measured in 4 mm tubes under similar conditions except for the number of scans. 400 scans were run on a-MEGO to obtain sufficient signal/noise ratio; only 40 scans were run on DPPH to avoid saturation. Double integrated areas of as-measured curves were normalized with the number of scans and mass of each sample. A concentration of  $\sim 2 \times 10^{16}$  spins/g was estimated for this a-MEGO sample, corresponding to a concentration of 0.4 spins per million carbon atoms.

## 7. XPS data for a-MEGO and analysis

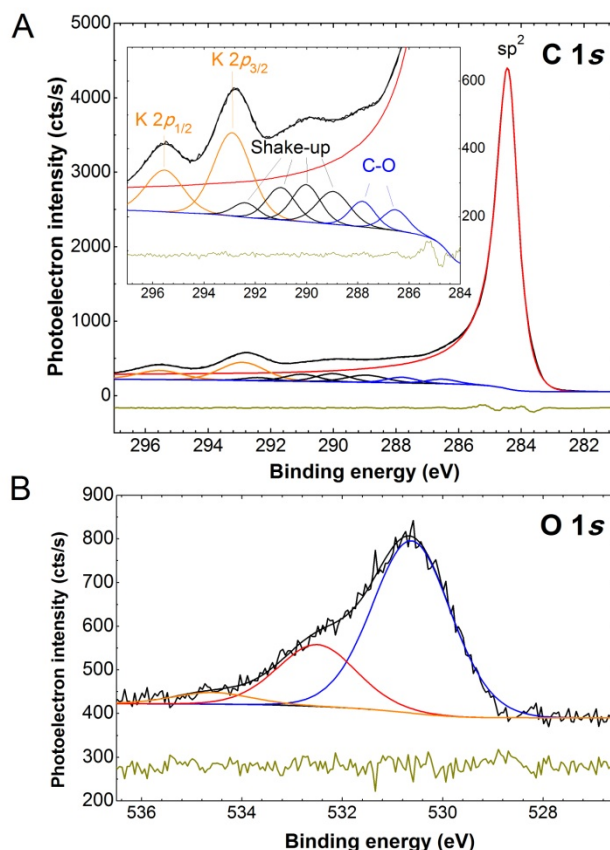


Fig. S4 Detailed XPS analysis of a-MEGO sample (SSA  $\sim 2520 \text{ m}^2/\text{g}$ ). (A) Fit to the C 1s region is shown, with detailed spectrum inset. The main  $sp^2$  carbon peak is a Doniach-Sunjić line with asymmetry parameter  $\alpha=0.20$  and FWHM 0.78 eV, which are reasonably close to values for these parameters in fits to highly oriented pyrolytic graphite (HOPG) and glassy carbon (7). Multiple states are also present on the high binding energy side of the main  $sp^2$  peak. An  $sp^3$  component, if present, is expected at +0.8 to +0.9 eV above the  $sp^2$  component in the C 1s spectrum (9). Attempts to fit the spectral envelope with an  $sp^3$  component indicate that  $sp^3$  carbon is below the limit of detection of XPS (approximately 1 at. %). Two C 1s states are observed at +2.0 and +3.3 eV above the main  $sp^2$  peak (with widths of 1.2 eV) and are attributed to C-O bonding with corresponding states observed in the O 1s and impurity K 2p spectra. Several shake-up features are also present at +4.4, +5.5, +6.5 and +7.9 eV above the main  $sp^2$  peak (widths of 1.5, 1.3, 1.3 and 1.1 eV

respectively) and are in good agreement with fits to the extended shake-up energy loss spectrum of glassy carbon and highly oriented pyrolytic graphite (HOPG) by Leiro et. al.(7). Residual potassium (< 2 at. %) from the KOH activation process is detected as a K  $2p$  doublet with the K  $2p_{3/2}$  state observed at 292.9 eV. (B) The O  $1s$  region is shown and composed of three components at 530.6 eV ( $K_2CO_3$ ), 532.5 eV ( $KHCO_3$ ) and 534.6 eV (KOH) (10-12). It is noted that the C  $1s$  shake up features described above make the unequivocal deconvolution of a carbonate bond problematic. Residual peak fitting error is shown beneath all spectra.

## 8. Raman and FTIR analysis of a-MEGO

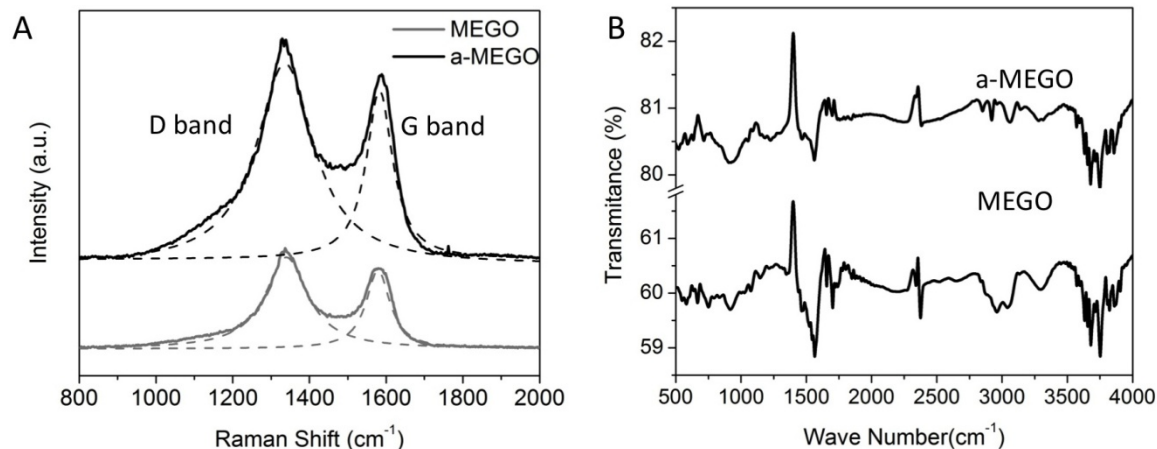


Fig. S5 (A) Raman of a-MEGO and MEGO control sample. The  $I_d/I_g$  slightly increases from  $\sim 1.16$  in MEGO to  $\sim 1.19$  in a-MEGO. From Lorentzian fitting, the D band FWHM increases from  $\sim 135$  to  $\sim 183$  cm<sup>-1</sup>. (B) FTIR transmittance spectra. The following bands were observed: O-H stretching (3200-3400 cm<sup>-1</sup>), C-H aliphatic (2800-3000 cm<sup>-1</sup>), C=O and C-O stretching (1640-1750 cm<sup>-1</sup>), aromatic C=C stretching (1400-1600 cm<sup>-1</sup>) and bands related to aromatic content (700-920 cm<sup>-1</sup>) such as out of plane C-H bending ( $\sim 910$  cm<sup>-1</sup>) with different degrees of substitution. Compared with the MEGO control sample, a-MEGO shows lower signals from the oxygen or hydrogen containing groups.

## 9. Comparison of N<sub>2</sub> BET data for MEGO and a-MEGO

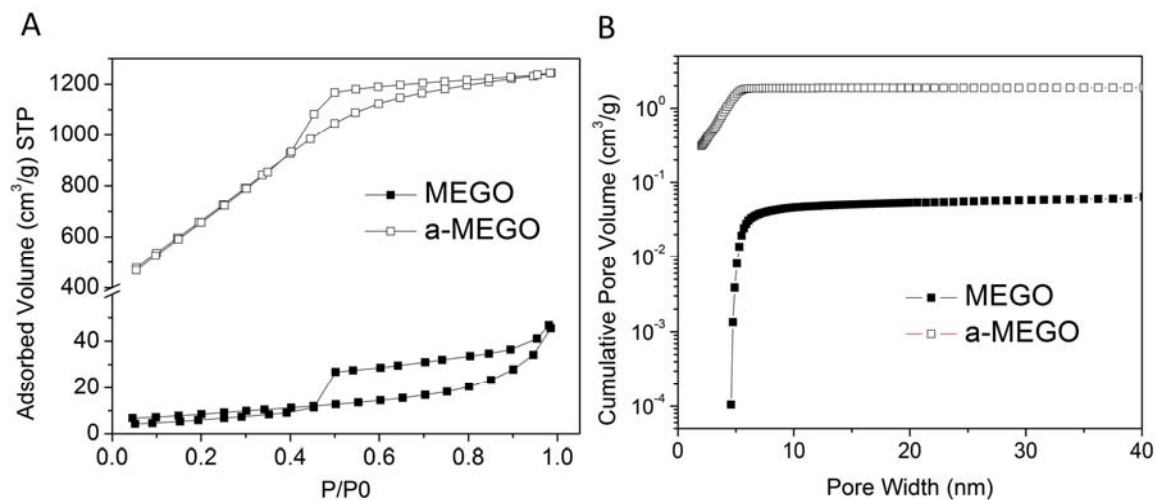


Fig. S6 N<sub>2</sub> adsorption/desorption analysis of a-MEGO ( $\sim 2520 \text{ m}^2/\text{g}$ ) with MEGO as control. (A) N<sub>2</sub> isotherm curves at 77.4 K. (B) Cumulative pore volume versus pore diameter plots obtained from the adsorption isotherm in (A). NLDFT analysis for carbon with slit/cylindrical model was used on the adsorption data to obtain the pore volumes.



## 10. QSDFT pore size distribution of a-MEGO

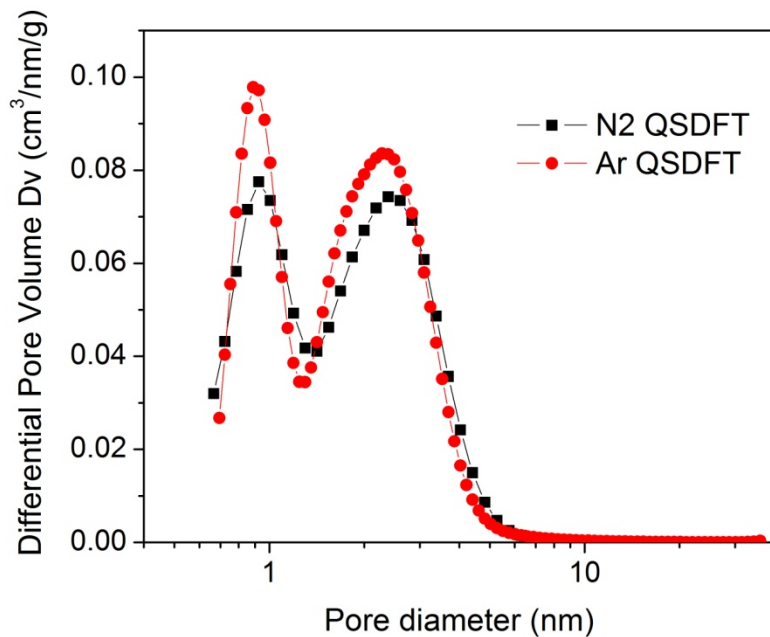


Fig S7 ‘Quenched solid density functional theory’ (QSDFT) pore size distribution of a-MEGO. In addition to the NLDFT pore size distribution shown in Fig. 3B (which was based on NLDFT assuming a slit/cylindrical pore hybrid model), we also analyzed the nitrogen (77.4 K) and argon (87.3 K) adsorption isotherms by assuming a slit pore model and QSDFT, which quantitatively accounts for the surface geometrical inhomogeneity. It follows that this pore size distribution essentially resembles the distribution from the slit/cylindrical pore model shown in the manuscript (Fig. 3 B); however, the mesopore size is slightly smaller in the slit pore QSDFT model.

## 11. Supercapacitor performance of a-MEGO with TEA BF<sub>4</sub>/AN electrolyte

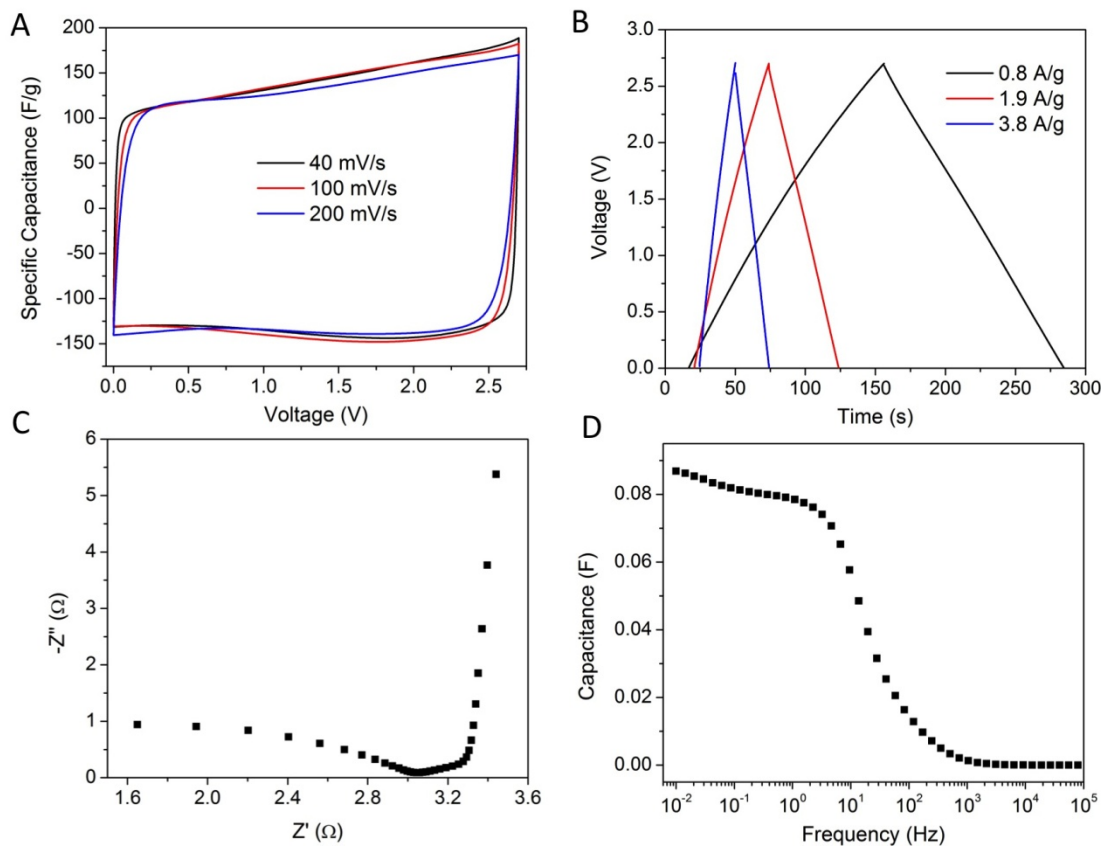


Fig. S8 Supercapacitor performance of a-MEGO (SSA  $\sim 3100 \text{ m}^2/\text{g}$ ) with 1.0 M TEA BF<sub>4</sub>/AN electrolyte. (A) CV curves for different scan rates. Rectangular shapes indicate the capacitive behavior. (B) Galvanostatic charge/discharge curves of a-MEGO based supercapacitor under different constant currents. The specific capacitances calculated from the discharge curves are 154, 145 and 141 F/g, for the constant currents of 0.8, 1.9 and 3.8 A/g, respectively. From the discharge data obtained at the constant current of 0.8 A/g, the energy density and power density were estimated as 39 Wh/kg and 145 kW/kg, respectively, when normalized with the total weight of two a-MEGO electrodes. (C) Nyquist plot, displaying a similar resistance as that of a-MEGO in BMIM BF<sub>4</sub>/AN electrolyte. (D) Frequency response of the capacitance of the a-MEGO supercapacitor.

## 12. Stability testing of supercapacitor having a-MEGO with BMIM BF<sub>4</sub> electrolyte

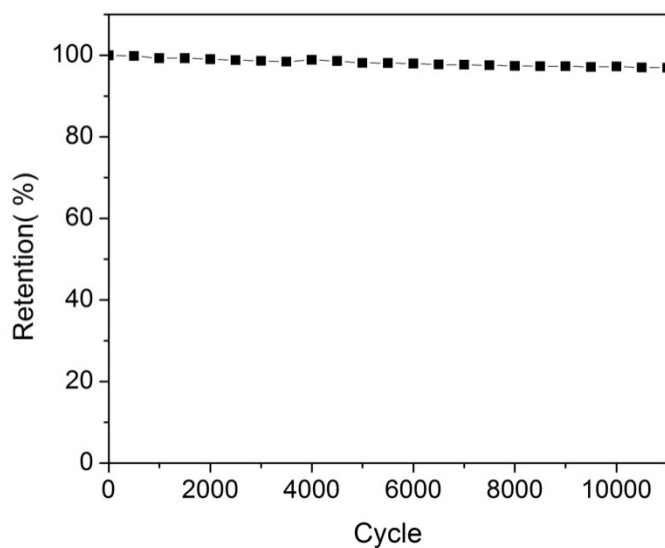


Fig. S9 Testing of the a-MEGO (with surface area of  $\sim 3100 \text{ m}^2/\text{g}$ ) based supercapacitor in neat BMIM BF<sub>4</sub> over 10000 cycles. Constant current cycles were run at a rate of 2.5 A/g. Retention of 97% was obtained after 10000 cycles. Here the pure IL was used as electrolyte to minimize possible contamination.

### 13. Supercapacitor performance of a-MEGO with EMIM TFSI electrolyte

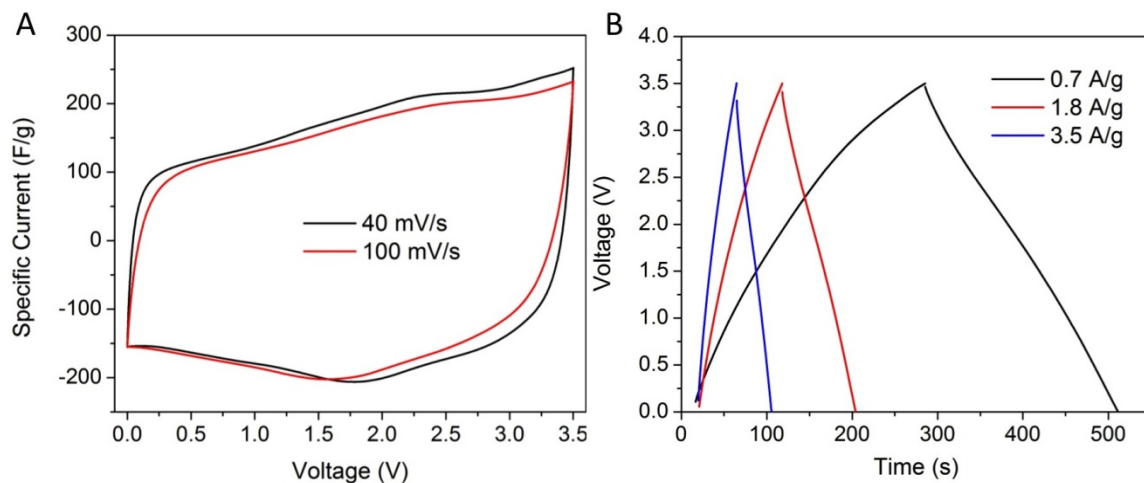


Fig. S10 Supercapacitor performance of a-MEGO (SSA  $\sim 3100 \text{ m}^2/\text{g}$ ) in neat EMIM TFSI electrolyte. (A) CV curves under different scan rates. (B) Galvanostatic charge/discharge curves under different constant currents. The specific capacitances calculated from the discharge curves with maximum voltage of 3.5 V are 200, 192 and 187 F/g for the currents of 0.7, 1.8 and 3.5 A/g, respectively. The normalized ESR is  $0.025 \Omega \cdot \text{g}$ . From the discharge data obtained at the constant current of 0.7 A/g, the energy density and power density were estimated as 85 Wh/kg and 122 kW/kg, when normalized with the total weight of the two a-MEGO electrodes.

#### 14. N<sub>2</sub> adsorption results of a-TEGO

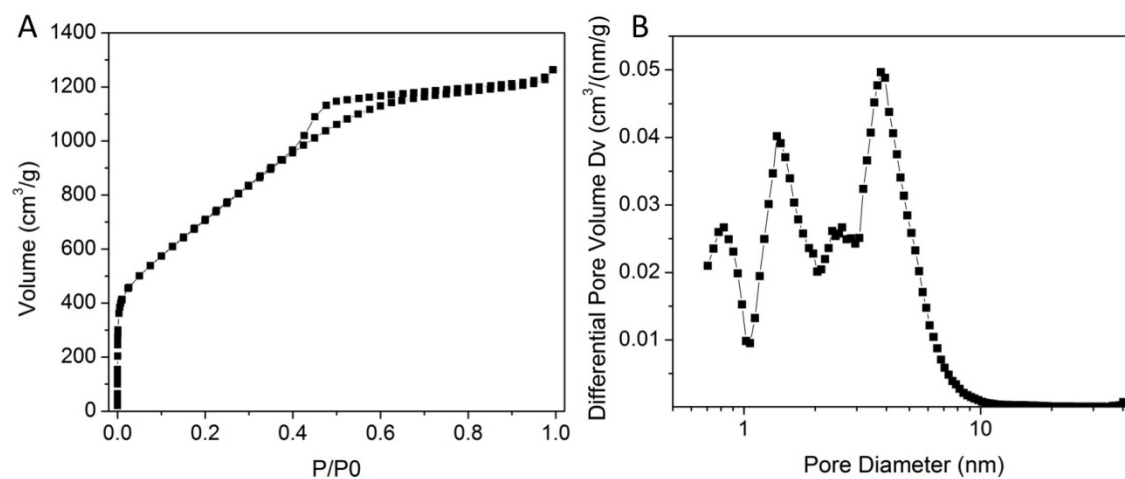


Fig. S11 N<sub>2</sub> adsorption/desorption analysis of a-TEGO. (A) High resolution, low pressure isotherm, from which a high BET SSA of 2675 m<sup>2</sup>/g (calculated in the linear relative pressure range from 0.1 to 0.3) is obtained. (B) Pore size distribution for N<sub>2</sub> adsorption (calculated using a slit/cylindrical NLDFT model).

## 15. Supercapacitor performance of a-TEGO with BMIM BF<sub>4</sub>/AN electrolyte

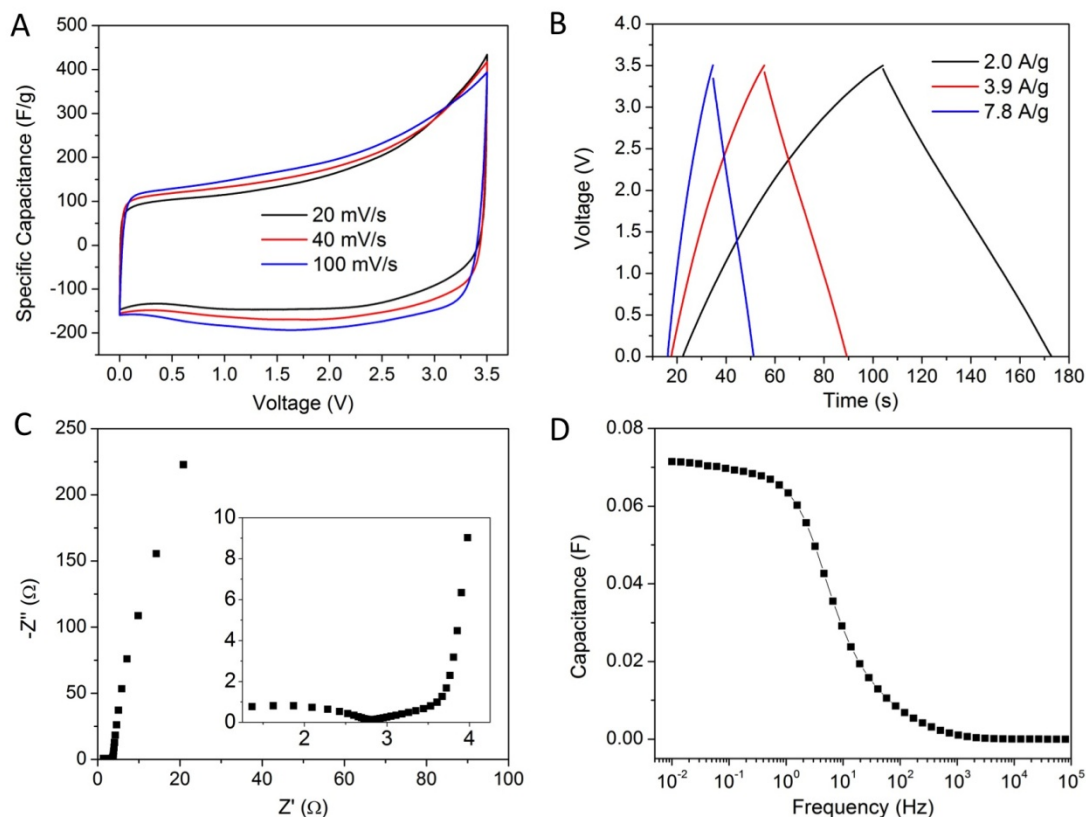


Fig. S12 Supercapacitor performance of a-TEGO (SSA  $\sim 2700 \text{ m}^2/\text{g}$ ) in the BMIM BF<sub>4</sub>/AN electrolyte. (A) CV curves for different scan rates. (B) Galvanostatic charge/discharge curves under different constant currents. The capacitance values calculated are 156, 154 and 154 F/g for the currents of 2.0, 3.9 and 7.8 A/g, respectively. From the discharge data obtained at the constant current of 2.0 A/g, the ESR, energy density and power density were estimated as 4.1  $\Omega$ , 66 Wh/kg and 282 kW/kg, respectively. (C) Nyquist plot for the a-TEGO based supercapacitor. (D) Frequency response of the capacitance of the a-TEGO supercapacitor in BMIM BF<sub>4</sub>/AN electrolyte.

## 16. Movies S1

Movies S1 Through-focal series high resolution TEM images of the a-MEGO structure. The images were obtained at 80 kV on the aberration corrected FEI Titan, with a focal step of  $-4$  nm per image. Initial focus is deliberately slightly over-focus, and scans through slightly under-focus, so that in a given frame some portion of the wedge-shaped sample is in exact / Scherzer defocus. The images show that the a-MEGO structure is composed of a high density of pores of very small size, with the pore walls being composed of single carbon sheets.

## 17. References

1. Y. Zhu *et al.*, *Carbon* **48**, 2118 (2010).
2. H. C. Schniepp *et al.*, *Journal of Physical Chemistry B* **110**, 8535 (2006).
3. S. D. Berger, D. R. McKenzie, P. J. Martin, *Philosophical Magazine Letters* **57**, 285 (1988).
4. H. Daniels, R. Brydson, B. Rand, A. Brown, *Philosophical Magazine* **87**, 4073 (2007).
5. R. Egerton, *Electron energy loss spectroscopy in the electron microscope*. (Plenum, New York, ed. 2nd, 1996).
6. S. Doniach, M. Sunjic, *Journal of Physics C: Solid State Physics* **3**, 285 (1970).
7. J. A. Leiro, M. H. Heinonen, T. Laiho, I. G. Batirev, *Journal of Electron Spectroscopy and Related Phenomena* **128**, 205 (2003).
8. M. D. Stoller, R. S. Ruoff, *Energy & Environmental Science* **3**, 1294 (2010).
9. R. Haerle, E. Riedo, A. Pasquarello, A. Baldereschi, *Physical Review B* **65**, 045101 (2001).
10. A. Shchukarev, D. Korolkov, *Central European Journal of Chemistry* **2**, 347 (2004).
11. P. M. Blass, X. L. Zhou, J. M. White, *The Journal of Physical Chemistry* **94**, 3054 (1990).
12. D. V. Chakarov, *et al.*, *Journal of Physics: Condensed Matter* **5**, 2903 (1993).